A KALMAN FILTER FOR MASS PROPERTY AND THRUST IDENTIFICATION OF THE SPIN-STABILIZED MAGNETOSPHERIC MULTISCALE FORMATION

Steven Z. Queen[(1)]
[(1)]*NASA/Godard Space Flight Center, Code 591, Greenbelt, MD 20771, USA,*
steven.z.queen@nasa.gov

Abstract: *The Magnetospheric Multiscale (MMS) mission consists of four identically instrumented, spin-stabilized observatories, elliptically orbiting the Earth in a tetrahedron formation. For the operational success of the mission, on-board systems must be able to deliver high-precision orbital adjustment maneuvers. On MMS, this is accomplished using feedback from on-board star sensors in tandem with accelerometers whose measurements are dynamically corrected for errors associated with a spinning platform. In order to determine the required corrections to the measured acceleration, precise estimates of attitude, rate, and mass-properties are necessary. To this end, both an on-board and ground-based Multiplicative Extended Kalman Filter (MEKF) were formulated and implemented in order to estimate the dynamic and quasi-static properties of the spacecraft.*

Keywords: *Kalman Filter, system identification, attitude estimation, calibration*

1 Introduction

The Magnetospheric Multiscale (MMS) mission, launched on March 13, 2015, is the fourth mission of NASA's Solar Terrestrial Probe program. MMS consists of four identically instrumented observatories that function as a formation to provide the first definitive study of magnetic reconnection in space.

Since it is frequently desirable to isolate electric and magnetic field sensors from stray effects caused by the spacecraft's core-body, the suite of instruments on MMS includes six radial and two axial instrument-booms with deployed lengths ranging from 5–60 meters (see Fig. 1). The observatory is spin-stabilized about its positive z-axis with a nominal rate slightly above 3 rev/min (RPM). The spin is also used to maintain tension in the four radial wire-booms.

Each observatory's Attitude Control System (ACS) is responsible for orbital adjustments, attitude control, and spin adjustments. Its sensor and actuator compliment consists of Adcole's spinning slit digital sun sensor, a four camera-head μASC Star Tracker System (STS) manufactured by the Technical University of Denmark, the micro-g resolution Acceleration Measurement System (AMS) produced by ZIN Technologies, and four axial AMPAC 1-lbf (4.4 N) and eight radial Aerojet 4-lbf (17.8 N) mono-propellant hydrazine thrusters. Additional details on the ACS hardware and maneuvering system controller may be found in the references[1][2].

The sections that follow describe the formulation and performance of the Multiplicative Extended Kalman Filter (MEKF) that is used for on-orbit attitude and rate determination, and the additional augmented filter-states and measurements necessary to perform an off-line mass property and thruster calibration. The paper concludes with a description of a calibration maneuver sequence performed with the spacecraft in a partially-deployed state, and a comparison of the system identification results against pre-flight expected values.

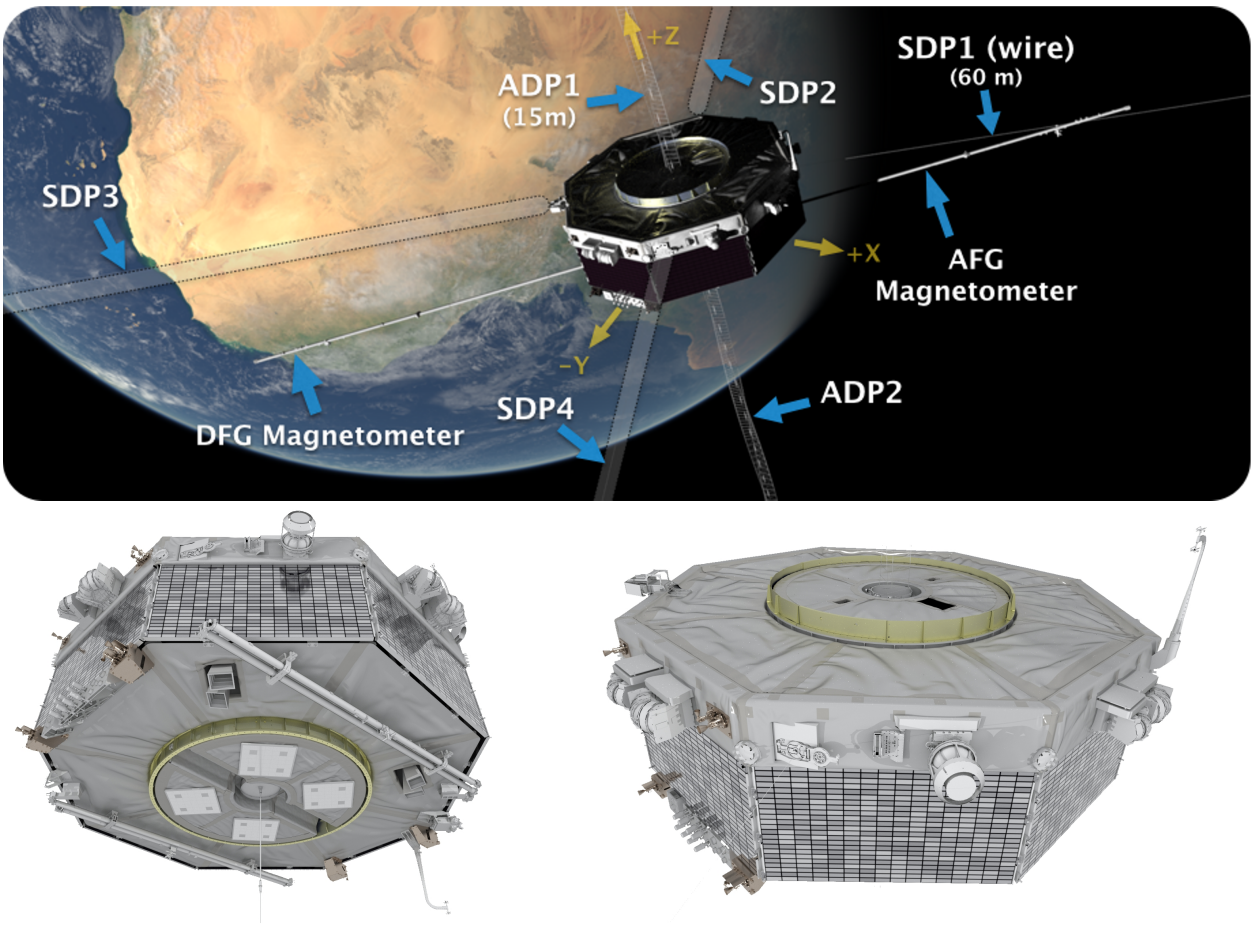

Figure 1. MMS Observatory Fully-Deployed (top) and Stowed (bottom)

2 Multiplicative Extended Kalman Filter (MEKF)

The MEKF is an evolved version of the Extended Kalman Filer (EKF) that was originally applied to the Space Precision Attitude Reference System (a.k.a. SPARS) in 1969, and has been rigorously developed by Lefferts, Markley, and Shuster[3][4][5]. It has frequently been used for spacecraft attitude determination, in both real-time and off-line systems. In particular, the MEKF addresses a pair of difficulties associated with using a quaternion in an Extended Kalman Filter—namely, preserving the four-component quaternion's unity norm constraint, while maintaining an unbiased estimate of the attitude. The fundamental idea of the MEKF is to use a quaternion as the "global" attitude, and use a three-component "local" representation for the attitude error (states) in the EKF. Whereas a more intuitive EKF approach might use all four elements of a error quaternion ($\Delta\mathbf{q}$) as states, and then perform a full-state update additively by $\mathbf{q}_{\text{true}} = \Delta\mathbf{q} + \hat{\mathbf{q}}$ (followed by an *ad hoc* normalization scheme), the MEKF advocates a multiplicative full-state update

$$\mathbf{q}_{\text{true}} = \delta\mathbf{q} \otimes \hat{\mathbf{q}} \tag{1}$$

where $\mathbf{q}_{\text{true}}$ is the quaternion parameterization of the true rotation/transformation from an inertially-fixed reference frame to a body-frame attached to the spacecraft, $\hat{\mathbf{q}}$ is the (unbiased) estimate of $\mathbf{q}_{\text{true}}$, and $\delta\mathbf{q}$ is an error quaternion that is parameterized by three states in the filter—the *error vector*, $\delta\boldsymbol{\theta}$. Note that $\mathbf{q}_{\text{true}}$, $\hat{\mathbf{q}}$, and $\delta\mathbf{q}$ are all properly normalized *unit quaternions*.

Also introduced in Eq. (1) is the notation for a (left) *quaternion product* that denotes a 4×4 matrix formed from a four element column-vector, that expands to

$$\mathbf{q}^{\otimes} \equiv \begin{bmatrix} q_1 \\ q_2 \\ q_3 \\ q_4 \end{bmatrix}^{\otimes} = \begin{bmatrix} \mathbf{q}_{1:3} \\ q_4 \end{bmatrix}^{\otimes} = q_4 \mathbb{I}_4 + \begin{bmatrix} -\mathbf{q}_{1:3}^{\times} & \mathbf{q}_{1:3} \\ -\mathbf{q}_{1:3}^{\mathsf{T}} & 0 \end{bmatrix} = \begin{bmatrix} q_4 \mathbb{I}_3 - \mathbf{q}_{1:3}^{\times} & \mathbf{q}_{1:3} \\ -\mathbf{q}_{1:3}^{\mathsf{T}} & q_4 \end{bmatrix} \tag{2}$$

with $\mathbf{q}_{1:3}$ denoting the vector part of the quaternion and q_4 the scalar element. This notation is analogous to the skew-symmetric matrix that is formed from a three-component base-vector, e.g. the angular rate vector $\boldsymbol{\omega}$, as

$$\boldsymbol{\omega}^{\times} \equiv \begin{bmatrix} \omega_x \\ \omega_y \\ \omega_z \end{bmatrix}^{\times} = \begin{bmatrix} 0 & -\omega_z & \omega_y \\ \omega_z & 0 & -\omega_x \\ -\omega_y & \omega_x & 0 \end{bmatrix} \tag{3}$$

that is equivalent to the *vector cross product* in matrix algebra. Lastly, the symbol $\mathbb{I}_n$ is used through the text to represent the *identity matrix* of dimension $n \times n$.

What exactly then is the error vector $\boldsymbol{\delta\theta}$ that appears in the filter? Well, for small errors, a 1st-order approximation is a legitimate abstraction—and the error states of a Kalman Filter are typically kept small. Conceptually, a perfectly adequate "mental picture" of $\boldsymbol{\delta\theta}$ is a vector of small error angles (e.g. θ_x,θ_y,θ_z). With that in mind, the 1st-order relationship between the error vector and the error quaternion is

$$\boldsymbol{\delta q} \equiv \mathbf{q}_{\mathsf{true}}^{\otimes} (\hat{\mathbf{q}}^{-})^{-1} \approx \begin{bmatrix} \frac{\boldsymbol{\delta\theta}}{2} \\ 1 \end{bmatrix} \tag{4}$$

which is now not of unit norm. However, even in the Kalman Filter's algorithm—one that is linear by design—a 1st-order approximation is an insufficient description of the error vector given that the ultimate goal is to systematically address concerns surrounding quaternion normalization and biased-estimates. For that purpose, a more precise definition of the filter's three-component error vector $\boldsymbol{\delta\theta}$ is needed. Fortunately, many rigorously defined three-component attitude representations are available to choose from—the *Euler rotation axis* and *Euler angle*, the *Gibbs vector* (a.k.a. *Rodrigues parameters*), *modified Rodrigues parameters*, *Tait-Bryan angles* (a.k.a. a 1-2-3 *Euler sequence*), etc.—each with their own benefits and pitfalls. Which particular parameterization is "best" is entirely a system design decision, and the references ([3],[4]) expound on the usage for each possible choice. In fact, the only places in the MEKF where the particular choice of parameterization (i.e. exact definition of $\boldsymbol{\delta\theta}$ beyond 1st-order) comes into play are the *measurement residual computation* and *reset operation*—both of which will be discussed shortly.

For MMS, the Gibb's vector ($\mathbf{g}$) was selected to be the three-component parameterization of the attitude error. It is related to the error quaternion by

$$\boldsymbol{\delta g} \equiv \frac{\boldsymbol{\delta q}_{1:3}}{\delta q_4} \tag{5}$$

or its inverse

$$\boldsymbol{\delta q} = \frac{\pm 1}{\sqrt{1+\|\boldsymbol{\delta g}\|^2}} \begin{bmatrix} \boldsymbol{\delta g} \\ 1 \end{bmatrix} \tag{6}$$

and to the error vector states by

$$\boldsymbol{\delta\theta} \equiv 2\boldsymbol{\delta g} \tag{7}$$

This error vector definition allows for a more precise re-statement of Eq. (4) as

$$\boldsymbol{\delta q} = \frac{1}{\sqrt{4+\|\boldsymbol{\delta\theta}\|^2}} \begin{bmatrix} \boldsymbol{\delta\theta} \\ 2 \end{bmatrix} = \begin{bmatrix} \dfrac{\boldsymbol{\delta\theta}}{2} + \ldots \mathscr{O}(\boldsymbol{\delta\theta}^3) \\ 1 - \frac{1}{8}\|\boldsymbol{\delta\theta}\|^2 + \ldots \mathscr{O}(\boldsymbol{\delta\theta}^3) \end{bmatrix} \tag{8}$$

The Gibbs vector parameterization is a mapping from four-dimension quaternion space to three-dimensional Euclidean space, and is infinity for 180-degree rotations (i.e. $q_4 = 0$). While not recommended as a global attitude representation, it has some nice properties when used in conjunction with the MEKF. These benefits include:

- free of singularities up to $\pm$180-degrees (error states will never be that large)
- avoids accumulation of numerical errors in the full-state quaternion norm through an explicit normalization in the "reset" that is neither an *ad hoc* re-normalization operation, nor does it require transcendental function evaluations (see Eq. (8))
- largest possible 180° attitude errors map to infinity, so the representation is conceptually compatible with a Gaussian (or other random distribution) with infinitely long tails
- observation model is insensitive to the sign ambiguity in the star camera's output quaternion
- although not unique to the Gibbs vector parameterization, the diagonals of the error covariance matrix (P) map directly to attitude error variance (σ^2)

To summarize, the attitude error-states ($\boldsymbol{\delta\theta}$) used in the MMS MEKF are equal to twice the Gibbs error-vector ($\boldsymbol{\delta g}$), and for "small" values are approximately the angle of rotation about each of the body-axes from the current full-state estimate ($\hat{\mathbf{q}}$) to the true attitude of the spacecraft ($\mathbf{q}_{\mathsf{true}}$).

2.1 Dynamical System Model (MMS ACS)

Armed with a better understanding of the nuances of the MEKF, we may now focus on the specifics of the MMS application. The attitude control system (ACS) flight software (FSW) is limited to the computational capabilities of the flight processor (Motorola RH-CF5208 Coldfire), which lacks hardware acceleration of floating-point operations. As a result, the ACS FSW models the spacecraft's angular rate ($\boldsymbol{\omega}$) dynamics using *Euler's rotational equation* of a simple rigid-body (even after all the boom appendages are deployed) that is driven by autonomously commanded ($\mathbf{u}(t)$) thruster torques ($\boldsymbol{\tau}(\mathbf{u})$).

$$\boldsymbol{\tau}(\mathbf{u}) = \mathbf{I}\dot{\boldsymbol{\omega}} + \boldsymbol{\omega}^{\times}\mathbf{I}\boldsymbol{\omega} \tag{9}$$

where $\mathbf{I}$ is the second mass moment matrix about the spacecraft's center of mass ($\mathbf{r}_c$). The true attitude kinematics are in turn driven by the angular rate.

$$\dot{\mathbf{q}} = \frac{1}{2}\begin{bmatrix}\boldsymbol{\omega}\\0\end{bmatrix}^{\otimes}\mathbf{q} \tag{10}$$

$$= \frac{1}{2}\begin{bmatrix}-\boldsymbol{\omega}^{\times} & \boldsymbol{\omega}\\ -\boldsymbol{\omega}^{\mathsf{T}} & 0\end{bmatrix}\begin{bmatrix}\mathbf{q}_{1:3}\\ q_4\end{bmatrix} \tag{11}$$

The commonly used *gyro substitution model*[4] is not an option for MMS due to the lack of an on-board gyroscope. Therefore, the angular rate (expressed in the body-frame) along with the attitude quaternion (from inertial to body-frame) make up the seven states of the dynamical system model that is the basis for the on-board MEKF.

As previously discussed, the MEKF operates on only six states of attitude and rate errors—the number is reduced by one using the error vector $\boldsymbol{\delta\theta}$ attitude parameterization. Since the *reset operation* (discussed in section 2.3) moves the error state information into the full-state after each measurement is processed, and the full-states are propagated using (non-linear) *Runge-Kutta* integration, the MMS MEKF does not ever perform an explicit propagation of its error states ($\hat{\mathbf{x}}$). However, the error-state covariance ($\mathbf{P}$) is propagated using linearized dynamics, so it is still necessary to determine the coefficients of the linearized (state-space) model.

For the non-attitude error states (e.g. $\boldsymbol{\omega}$), the linearization process follows the standard EKF template[11]. The non-linear system dynamics ($\dot{\mathbf{x}} = \mathbf{f}(\mathbf{x},\mathbf{u},t)$) are expanded about a reference trajectory (i.e. the current state estimate $\hat{\mathbf{x}}(t)$), using a first-order *Taylor series* expansion to obtain the error-state dynamics

$$\overbrace{\mathbf{f}(\mathbf{x}(t),\mathbf{u}(t),t)}^{\dot{\mathbf{x}}} \approx \overbrace{\mathbf{f}(\hat{\mathbf{x}}(t),\mathbf{u}(t),t)}^{\dot{\hat{\mathbf{x}}}} + \left.\frac{\partial \mathbf{f}}{\partial \mathbf{x}}\right|_{\hat{\mathbf{x}},\mathbf{u}} \overbrace{(\mathbf{x}-\hat{\mathbf{x}})}^{\delta x} \tag{12}$$

$$\dot{\mathbf{x}} - \dot{\hat{\mathbf{x}}} \approx \left.\frac{\partial \mathbf{f}}{\partial \mathbf{x}}\right|_{\hat{\mathbf{x}},\mathbf{u}} \boldsymbol{\delta}\mathbf{x} \tag{13}$$

$$\boldsymbol{\delta}\dot{\mathbf{x}} \approx \mathbf{F}(t)\,\boldsymbol{\delta}\mathbf{x} \tag{14}$$

In the case of the spacecraft angular rate error, we have

$$\dot{\boldsymbol{\omega}} = \mathbf{f}_{\omega} = \mathbf{I}^{-1}\left[\boldsymbol{\tau}(\mathbf{u}) - \boldsymbol{\omega}^{\times}\mathbf{I}\boldsymbol{\omega}\right] \tag{15}$$

$$\boldsymbol{\delta}\dot{\boldsymbol{\omega}} = \left.\frac{\partial \mathbf{f}_{\omega}}{\partial \mathbf{x}}\right|_{\hat{\mathbf{q}},\hat{\boldsymbol{\omega}},\mathbf{u}} \boldsymbol{\delta}\mathbf{x} \tag{16}$$

$$= \left[\underbrace{\frac{\partial \mathbf{f}_{\omega}}{\partial \mathbf{q}}}_{\mathbf{0}_{3\times 3}} \cdot \frac{\partial \mathbf{q}}{\partial\,(\boldsymbol{\delta\theta})} \quad \frac{\partial \mathbf{f}_{\omega}}{\partial \boldsymbol{\omega}}\right]_{\hat{\mathbf{q}},\hat{\boldsymbol{\omega}},\mathbf{u}} \begin{bmatrix}\boldsymbol{\delta\theta}\\ \boldsymbol{\delta\omega}\end{bmatrix} \tag{17}$$

Recalling that the partial derivative of a scalar with respect to a vector is a vector, and that the partial derivative of a vector with respect to a vector is a matrix, we very much want to avoid taking the partial derivative of a matrix with respect to a vector (a hyper-matrix?)! With this in mind, a

matrix-equivalent to the vector cross product identity $\vec{u} \times \vec{v} = -\vec{v} \times \vec{u}$ is used along with the *chain rule* to evaluate the partial derivative of *Euler's equation* with respect to the angular rate—careful to always keep the vector being differentiated on the far-right of each compound term so that it drops out as the identity matrix.

$$\begin{aligned} \frac{\partial\left(\mathbf{I}\dot{\boldsymbol{\omega}}\right)}{\partial\boldsymbol{\omega}} &= -\frac{\partial\left(\boldsymbol{\omega}^{\times}\mathbf{I}\boldsymbol{\omega}\right)}{\partial\boldsymbol{\omega}} \\ &= -\frac{\partial\left(\boldsymbol{\omega}^{\times}\right)}{\partial\boldsymbol{\omega}}\mathbf{I}\boldsymbol{\omega} - \boldsymbol{\omega}^{\times}\frac{\partial\left(\mathbf{I}\boldsymbol{\omega}\right)}{\partial\boldsymbol{\omega}} \\ &= \left(\mathbf{I}\boldsymbol{\omega}\right)^{\times}\frac{\partial\boldsymbol{\omega}}{\partial\boldsymbol{\omega}} - \boldsymbol{\omega}^{\times}\mathbf{I}\frac{\partial\boldsymbol{\omega}}{\partial\boldsymbol{\omega}} \end{aligned} \tag{18}$$

which yields the following linearization for use in the angular rate error dynamics of Eq. (17),

$$\frac{\partial\mathbf{f}_{\omega}}{\partial\boldsymbol{\omega}} = \mathbf{I}^{-1}\left[\left(\mathbf{I}\boldsymbol{\omega}\right)^{\times} - \boldsymbol{\omega}^{\times}\mathbf{I}\right] \tag{19}$$

Unfortunately, the additive error definition ($\boldsymbol{\delta}\mathbf{x} \equiv \mathbf{x} - \hat{\mathbf{x}}$) of Eq. (12) defeats the stated purpose of the MEKF (i.e. multiplicative update), and deriving the dynamics for the attitude-error requires traveling along a somewhat longer path. One route, taken by [4] and [5], begins by using the *chain rule* to obtain the time derivative of the attitude error definition of Eq. (1),

$$\frac{d}{dt}\left(\mathbf{q}_{\mathsf{true}} = \boldsymbol{\delta}\mathbf{q}^{\otimes}\hat{\mathbf{q}}\right) \tag{20}$$

$$\begin{aligned} \dot{\mathbf{q}}_{\mathsf{true}} &= \boldsymbol{\delta}\dot{\mathbf{q}}^{\otimes}\hat{\mathbf{q}} + \boldsymbol{\delta}\mathbf{q}^{\otimes}\dot{\hat{\mathbf{q}}} \\ \frac{1}{2}\begin{bmatrix}\boldsymbol{\omega}_{\mathsf{true}}\\ 0\end{bmatrix}^{\otimes}\mathbf{q}_{\mathsf{true}} &= \boldsymbol{\delta}\dot{\mathbf{q}}^{\otimes}\hat{\mathbf{q}} + \boldsymbol{\delta}\dot{\mathbf{q}}^{\otimes}\frac{1}{2}\begin{bmatrix}\hat{\boldsymbol{\omega}}\\ 0\end{bmatrix}^{\otimes}\hat{\mathbf{q}} \\ \frac{1}{2}\begin{bmatrix}\hat{\boldsymbol{\omega}}+\boldsymbol{\delta}\boldsymbol{\omega}\\ 0\end{bmatrix}^{\otimes}\boldsymbol{\delta}\mathbf{q}^{\otimes}\hat{\mathbf{q}} &= \boldsymbol{\delta}\dot{\mathbf{q}}^{\otimes}\hat{\mathbf{q}} + \boldsymbol{\delta}\dot{\mathbf{q}}^{\otimes}\frac{1}{2}\begin{bmatrix}\hat{\boldsymbol{\omega}}\\ 0\end{bmatrix}^{\otimes}\hat{\mathbf{q}} \end{aligned} \tag{21}$$

Right-multiplying Eq. (21) by $\hat{\mathbf{q}}^{-1}$ and rearranging yields

$$\boldsymbol{\delta}\dot{\mathbf{q}} = \frac{1}{2}\left\{\begin{bmatrix}\hat{\boldsymbol{\omega}}+\boldsymbol{\delta}\boldsymbol{\omega}\\ 0\end{bmatrix}^{\otimes}\boldsymbol{\delta}\mathbf{q} - \boldsymbol{\delta}\mathbf{q}^{\otimes}\begin{bmatrix}\hat{\boldsymbol{\omega}}\\ 0\end{bmatrix}\right\} \tag{22}$$

$$= \frac{1}{2}\left\{\begin{bmatrix}\hat{\boldsymbol{\omega}}+\boldsymbol{\delta}\boldsymbol{\omega}\\ 0\end{bmatrix}^{\otimes}\boldsymbol{\delta}\mathbf{q} - \begin{bmatrix}\hat{\boldsymbol{\omega}}\\ 0\end{bmatrix}^{\odot}\boldsymbol{\delta}\mathbf{q}\right\} \tag{23}$$

$$\begin{aligned} &= \frac{1}{2}\left\{\begin{bmatrix}-\hat{\boldsymbol{\omega}}^{\times} & \hat{\boldsymbol{\omega}}\\ \hat{\boldsymbol{\omega}}^{\mathsf{T}} & 0\end{bmatrix} - \begin{bmatrix}\hat{\boldsymbol{\omega}}^{\times} & \hat{\boldsymbol{\omega}}\\ \hat{\boldsymbol{\omega}}^{\mathsf{T}} & 0\end{bmatrix}\right\}\boldsymbol{\delta}\mathbf{q} + \frac{1}{2}\begin{bmatrix}\boldsymbol{\delta}\boldsymbol{\omega}\\ 0\end{bmatrix}^{\otimes}\boldsymbol{\delta}\mathbf{q} \\ &= \begin{bmatrix}-\hat{\boldsymbol{\omega}}^{\times} & 0\\ 0 & 0\end{bmatrix}\begin{bmatrix}\boldsymbol{\delta}\mathbf{q}_{1:3}\\ \delta q_4\end{bmatrix} + \frac{1}{2}\begin{bmatrix}-\boldsymbol{\delta}\boldsymbol{\omega}^{\times} & \boldsymbol{\delta}\boldsymbol{\omega}\\ -\boldsymbol{\delta}\boldsymbol{\omega}^{\mathsf{T}} & 0\end{bmatrix}\begin{bmatrix}\boldsymbol{\delta}\mathbf{q}_{1:3}\\ \delta q_4\end{bmatrix} \end{aligned}$$

$$= \begin{bmatrix}-\boldsymbol{\omega}^{\times}\boldsymbol{\delta}\mathbf{q}_{1:3} - \frac{1}{2}\boldsymbol{\delta}\boldsymbol{\omega}^{\times}\boldsymbol{\delta}\mathbf{q}_{1:3} + \frac{1}{2}\delta q_4\boldsymbol{\delta}\boldsymbol{\omega}\\ -\frac{1}{2}\boldsymbol{\delta}\boldsymbol{\omega}^{\mathsf{T}}\boldsymbol{\delta}\mathbf{q}_{1:3}\end{bmatrix} \tag{24}$$

In Eq. (23) the quaternion identity $\mathbf{p}\otimes\mathbf{q}=\mathbf{q}\odot\mathbf{p}$ was used[4], which introduces here the "left" quaternion multiplication matrix notation, $[]^{\odot}$. The left-product is defined identically to the right-product (Eq, (2)) except for the sign on the cross-product term in the upper-left 3×3 block of the matrix. The expressions of Eqs. (22) – (24) for attitude error-quaternion are wonderfully exact. However there are two problems—the quaternion is not the final attitude-error parameterization that will be used in the filter, and it is non-linear in the error-states. In order to make the change of variables and linearize the error-state dynamics, the 1st-order approximations $\delta\mathbf{q}_{1:3}\approx\delta\boldsymbol{\theta}/2$ and $\delta q_4=1$ (see Eq. (4)) are used for the error-vector, and terms that are the product of two (small) error-states are dropped ($\delta\boldsymbol{\omega}\delta\boldsymbol{\theta}\approx\mathbf{0}$). With these substitutions, Eq. (24) becomes

$$\begin{bmatrix}\dfrac{\delta\dot{\boldsymbol{\theta}}}{2}\\ 0\end{bmatrix}\approx\begin{bmatrix}-\frac{1}{2}\boldsymbol{\omega}^{\times}\delta\boldsymbol{\theta}+\frac{1}{2}\delta\boldsymbol{\omega}\\ 0\end{bmatrix}$$

$$\delta\dot{\boldsymbol{\theta}}\approx-\boldsymbol{\omega}^{\times}\delta\boldsymbol{\theta}+\delta\boldsymbol{\omega} \tag{25}$$

which is the desired final form of the error vector dynamics. The dynamics for the full and error states of the ACS flight software MEKF are summarized in Table 1.

Table 1. Summary of State Dynamics for MMS On-board MEKF

Nonlinear Full-State Model	Linearized Error-State Model
$\dot{\mathbf{x}}(t)=\mathbf{f}(\mathbf{q}(t),\boldsymbol{\omega}(t),\mathbf{u}(t),\mathbf{w}(t))$ $=\begin{Bmatrix}\mathbf{f}_q(\mathbf{q},\boldsymbol{\omega})\\ \mathbf{f}_{\omega}(\boldsymbol{\omega},\mathbf{u})\end{Bmatrix}+G\mathbf{w}$ $\begin{Bmatrix}\dot{\mathbf{q}}\\ \dot{\boldsymbol{\omega}}\end{Bmatrix}=\begin{Bmatrix}\frac{1}{2}\begin{bmatrix}-\boldsymbol{\omega}^{\times} & \boldsymbol{\omega}\\ -\boldsymbol{\omega}^{\mathsf{T}} & 0\end{bmatrix}\mathbf{q}\\ \mathbf{I}^{-1}\left[\boldsymbol{\tau}(\mathbf{u})-\boldsymbol{\omega}^{\times}\mathbf{I}\boldsymbol{\omega}\right]\end{Bmatrix}+G\mathbf{w}$	$\delta\dot{\mathbf{x}}=\mathbf{f}(\delta\boldsymbol{\theta}(t),\delta\boldsymbol{\omega}(t),\mathbf{u}(t),\mathbf{w}(t))$ $=\begin{Bmatrix}\mathbf{f}_{\theta}(\delta\boldsymbol{\theta},\delta\boldsymbol{\omega})\\ \mathbf{f}_{\omega}(\delta\boldsymbol{\omega},\mathbf{u})\end{Bmatrix}+G(t)\mathbf{w}$ $\begin{bmatrix}\delta\dot{\boldsymbol{\theta}}\\ \delta\dot{\boldsymbol{\omega}}\end{bmatrix}\approx\begin{bmatrix}-\hat{\boldsymbol{\omega}}^{\times} & \mathbb{I}_3\\ \mathbf{0}_{3\times 3} & \mathbf{I}^{-1}\left[(\mathbf{I}\hat{\boldsymbol{\omega}})^{\times}-\hat{\boldsymbol{\omega}}^{\times}\mathbf{I}\right]\end{bmatrix}\begin{bmatrix}\delta\boldsymbol{\theta}\\ \delta\boldsymbol{\omega}\end{bmatrix}+\begin{bmatrix}\mathbf{w}_{\theta}\\ \mathbf{w}_{\omega}\end{bmatrix}$ $\approx F(t)\,\delta\mathbf{x}+\mathbf{w}$
Process Noise: $\mathbf{w}(t)\sim N(\mathbf{0},\mathbf{Q}(t))$	

2.2 Measurement Update

There are three sensors on the MMS observatories—a sun sensor (DSS), a star tracker (STS), and an accelerometer (AMS). Of the three, only the STS is used for on-board (real-time) attitude and rate determination. The DSS is excluded because its resolution of $\pm 0.125^{\circ}$ (450 arcsec) was shown to contribute little to the solution. The AMS acceleration measurements are neglected because of the modest capability of the flight processor (the filter would need to be augmented with bias states), and the additional power demands (AMS electronics plus thermal control heaters for bias stability). Nevertheless, the AMS is enabled for maneuvers, and the richness of information contained in its 1 kHz stream of μg acceleration measurements makes it possible to perform off-line system

calibration using ground-telemetered data (the subject of the second-half of this paper). The STS and AMS measurements are staggered in time, so there are no update issues with simultaneous measurements.

The specific form of the MEKF used on MMS is sometimes referred to as a *Continuous-Discrete Extended Kalman Filter*[6], due to the discrete measurement updates from the on-board sensors combined with the continuous state-dynamics. The generalized nonlinear observation model is

$$\mathbf{y}_k = \mathbf{h}\left(\mathbf{q}_{\mathsf{true}}(t_k), \boldsymbol{\omega}_{\mathsf{true}}(t_k), \ldots\right)_k + \mathbf{v}_k \tag{26}$$

where $\mathbf{v}_k$ is a vector of Gaussian distributed random measurement errors with covariance matrix R_k.

The goal of the measurement update is to use feedback of the difference between the actual (noisy) measurement $\mathbf{y}_k$ and a prediction of what it "should be" (i.e. its expected value $\hat{\mathbf{y}}_k$) in order to adjust the estimate using an optimal feedback gain (K_k). In the parlance of a Kalman filter with discrete measurements, this is called the *state update*, and K_k is the *Kalman gain*. This operation—which was described verbosely in the preceding paragraph—can be expressed more succinctly and elegantly with the following mathematical statement

$$\boldsymbol{\delta}\mathbf{x}_k^+ = \boldsymbol{\delta}\mathbf{x}_k^- + K_k\left\{\mathbf{y}_k - \hat{\mathbf{y}}_k\right\} \tag{27}$$

where the Kalman gain used is in the EKF standard form

$$K_k = P_k^- H_k^{\mathsf{T}}\left[H_k P_k^- H_k^{\mathsf{T}} + R\right]^{-1} \tag{28}$$

Furthermore, in an EKF, the measurement model is allowed to be a nonlinear function of the states, and is historically segregated into two parts using a 1st-order *Taylor series* approximation

$$\hat{\mathbf{y}}_k = E\left\{\mathbf{y}_k\right\} = E\left\{\mathbf{h}_k\left(\mathbf{x}_{\mathsf{true}}\right)\right\} \tag{29}$$

$$\approx \mathbf{h}_k\left(\hat{\mathbf{x}}_k\right) + \left.\frac{\partial \mathbf{h}}{\partial \mathbf{x}}\right|_{\hat{\mathbf{x}}_k}\left[\left(\mathbf{x}_{\mathsf{true}}\right)_k - \hat{\mathbf{x}}_k\right] \tag{30}$$

$$\approx \mathbf{h}_k\left(\hat{\mathbf{x}}_k\right) + H_k\left(\hat{\mathbf{x}}_k\right)\boldsymbol{\delta}\mathbf{x}_k \tag{31}$$

where H_k is known as the *measurement sensitivity matrix*—conceptually a local gradient in the nonlinear measurement with respect to a particular state. While this is pedestrian fare for a standard EKF, it has been made explicit here because it is another instance in the MEKF where the attitude error-state must be handled carefully. Specifically, for the additive states it is immaterial whether or not the sensitivity is with respect to the full or error state (i.e. the partial with respect to $\mathbf{x}$ produces the same result as the partial with respect to $\boldsymbol{\delta}\mathbf{x}$). Not so for the multiplicative attitude! It requires a more precise statement of the gradient. Since the linearized "slope" of the partial derivative multiplies the error states in Eq. (31), the measurement sensitivity matrix (H_k) is correctly defined with respect to error states. However, for the remainder of the paper the sensitivity partials of the additive states will still appear as $\partial\mathbf{x}$ (i.e. with respect to a full-state), solely because $\partial\left(\boldsymbol{\delta}\mathbf{x}\right)$ is cumbersome notation. With that said, the definition of the measurement sensitivity matrix for the MMS on-board MEKF can be written as

$$H_k \equiv \left[\frac{\partial \mathbf{h}}{\partial \mathbf{q}} \cdot \frac{\partial \mathbf{q}}{\partial\left(\boldsymbol{\delta\theta}\right)} \qquad \frac{\partial \mathbf{h}}{\partial \boldsymbol{\omega}}\right]_{\hat{\mathbf{q}}_k, \hat{\boldsymbol{\omega}}} \tag{32}$$

where it can be shown[4] by using the 1st-order approximation of Eq. (4) produces the matrix

$$\frac{\partial \mathbf{q}_{\mathsf{true}}}{\partial(\delta\boldsymbol{\theta})} \approx \frac{\partial}{\partial(\delta\boldsymbol{\theta})}\left(\hat{\mathbf{q}}^{\odot}\begin{bmatrix}\frac{\delta\boldsymbol{\theta}}{2}\\1\end{bmatrix}\right) = \frac{1}{2}\begin{bmatrix}\hat{q}_4\,\mathbb{I}_3 + \hat{\mathbf{q}}_{1:3}^{\times}\\ -\hat{\mathbf{q}}_{1:3}^{\mathsf{T}}\end{bmatrix} \tag{33}$$

Finally, combining Eqs. (27) and (31) results in a state update for the kth measurement in the standard EKF form

$$\begin{bmatrix}\delta\boldsymbol{\theta}_k^+\\ \delta\boldsymbol{\omega}_k^+\end{bmatrix} = \begin{bmatrix}\delta\boldsymbol{\theta}_k^-\\ \delta\boldsymbol{\omega}_k^-\end{bmatrix} + K_k\overbrace{\left\{\mathbf{y}_k - \mathbf{h}\left(\hat{\mathbf{q}}_k^-,\hat{\boldsymbol{\omega}}_k^-\right) - H_k\left(\hat{\mathbf{q}}_k^-,\hat{\boldsymbol{\omega}}_k^-\right)\begin{bmatrix}\delta\boldsymbol{\theta}_k^-\\ \delta\boldsymbol{\omega}_k^-\end{bmatrix}\right\}}^{\boldsymbol{\rho}_k} \tag{34}$$

where $\boldsymbol{\rho}_k$ is referred to as the *measurement residual*. In the sections that follow, specific models are developed for the star tracker and accelerometer discrete measurement updates.

2.2.1 Star Sensor Measurements

The output of the MMS star tracker is simply a single quaternion per camera head unit ($\mathbf{q}_{\mathsf{chu}}$). Because it is important that the measurement $\mathbf{y}_k$ closely matches the estimated measurement $\hat{\mathbf{y}}_k$ in the residual calculation, the approximation of Eq. (33) is not used in favor of a measurement model that exactly matches our (Gibbs vector) parameterization of the attitude error. Specifically, the STS measurement model is

$$\begin{aligned}(\mathbf{y}_{\mathsf{chu}})_k = (\mathbf{h}_{\mathsf{chu}})_k &= \delta\boldsymbol{\theta}_k + (\mathbf{v}_{\mathsf{chu}})_k && (35)\\ &= (\delta\boldsymbol{\theta}_{\mathsf{chu}})_k && (36)\\ &= 2\frac{(\delta\mathbf{q}_{1:3})_k}{(\delta q_4)_k} \qquad \left(\approx 2\,(\delta\mathbf{q}_{1:3})_k \cdot \operatorname{sign}(\delta q_4)_k\right) && (37)\\ &= 2\frac{\left((\mathbf{q}_{\mathsf{chu}})_k^{\otimes}\,\hat{\mathbf{q}}_k^{-1}\right)_{1:3}}{\left((\mathbf{q}_{\mathsf{chu}})_k^{\otimes}\,\hat{\mathbf{q}}_k^{-1}\right)_4} && (38)\end{aligned}$$

which possesses the previously mentioned benefit of insensitivity to sign ambiguity in the star tracker output. The associated measurement sensitivity matrix is then

$$H_{\mathsf{chu}} = \left[\frac{\partial \mathbf{h}_{\mathsf{chu}}}{\partial(\delta\boldsymbol{\theta})} \quad \frac{\partial \mathbf{h}_{\mathsf{chu}}}{\partial\boldsymbol{\omega}}\right]_{\hat{\mathbf{q}}_k,\hat{\boldsymbol{\omega}}} = \begin{bmatrix}\mathbb{I}_3 & \mathbf{0}_{3\times 3}\end{bmatrix} \tag{39}$$

and the star tracker measurement residual itself is

$$\begin{aligned}(\boldsymbol{\rho}_{\mathsf{chu}})_k &= (\mathbf{y}_{\mathsf{chu}})_k - \mathbf{h}\left(\hat{\mathbf{q}}_k^-,\hat{\boldsymbol{\omega}}_k^-\right) - H_{\mathsf{chu}}\begin{bmatrix}\delta\boldsymbol{\theta}_k^-\\ \delta\boldsymbol{\omega}_k^-\end{bmatrix} && (40)\\ &= 2\frac{\left((\mathbf{q}_{\mathsf{chu}})_k^{\otimes}\,\hat{\mathbf{q}}_k^{-1}\right)_{1:3}}{\left((\mathbf{q}_{\mathsf{chu}})_k^{\otimes}\,\hat{\mathbf{q}}_k^{-1}\right)_4} - \underbrace{2\frac{\left(\hat{\mathbf{q}}_k^{\otimes}\hat{\mathbf{q}}_k^{-1}\right)_{1:3}}{\left(\hat{\mathbf{q}}_k^{\otimes}\hat{\mathbf{q}}_k^{-1}\right)_4}}_{\mathbf{0}_{3\times 1}} - \begin{bmatrix}\mathbb{I}_3 & \mathbf{0}_{3\times 3}\end{bmatrix}\begin{bmatrix}\delta\boldsymbol{\theta}_k^-\\ \delta\boldsymbol{\omega}_k^-\end{bmatrix} && (41)\\ &= (\delta\boldsymbol{\theta}_{\mathsf{chu}})_k - \delta\boldsymbol{\theta}_k^- && (42)\end{aligned}$$

Additionally, as will be explained shortly, the reset operation ensures $\delta\boldsymbol{\theta}_k^-$ is always zero.

For improved computational efficiency, the MMS ACS FSW combines the four simultaneous camera head unit observations into a single measurement to be processed by the MEKF[7]. This "effective" measurement is just the individual camera head residuals weighted by their associated *measurement covariance matrix* R^n_{chu} (transformed in to a common frame). This approach is tractable because all four measurements share a common sensitivity matrix H_{chu}.

$$(R_{\mathsf{eff}})_k = \left(\sum_{n=1}^{4} (R^n_{\mathsf{chu}})^{-1}_k \right)^{-1} \tag{43}$$

$$(\mathbf{y}_{\mathsf{eff}})_k = (R_{\mathsf{eff}})_k \sum_{n=1}^{4} (R^n_{\mathsf{chu}})^{-1}_k \, (\boldsymbol{\delta\theta}^n_{\mathsf{chu}})_k \tag{44}$$

On-board MMS, the measurement covariance matrix $R_k = E\left\{\mathbf{v}_k \mathbf{v}_k^{\mathsf{T}}\right\}$ is calculated one of two ways. It is either a time-varying matrix that is constructed from the CHU's internal algorithm's reported image fit-residual (a single scalar unsigned byte), or else it is a constant (diagonal) matrix loaded into the FSW. The latter was originally based upon the DTU STS performance specification ($\sigma_\perp = 20$, $\sigma_{\mathsf{boresite}} = 60$ arcsec), and then later tuned to the statistics of the actual flight residuals. Of the two methods, the fixed R approached proved to be more accurate.

The ensemble-average of the star camera head solutions essentially defines the spacecraft's body-frame. The knowledge error with regard to the alignment of the heads (relative to their nominal design and verified by ground metrology) is handled by the separate off-line calibration system known as the MMS Attitude Ground System. The goal of that calibration is to minimize persistent biases from the measurement residuals by adjusting the alignment estimate of each CHU. Details of the calibration process can be found in [8].

2.2.2 Accelerometer Measurements

The high-performance, tri-axial, acceleration measurement system (AMS) manufactured by ZIN technologies exists on the observatories in order to perform precise closed-loop orbital adjustments of the MMS formation[1][9]. However, the AMS's high-rate sensor data is also available to perform off-line system identification. Without delving too deeply in the derivation provided in [1], we can import the final form of the sampled acceleration measurement model

$$(\mathbf{y}_{\mathsf{ams}})_k = \mathbf{h}_{\mathsf{ams}}\left(\mathbf{f}_{\mathsf{thr}}, \mathbf{r}_c, \boldsymbol{\omega}, \mathbf{b}\right)_k \tag{45}$$

$$\mathbf{a}_k = \frac{\mathbf{f}_{\mathsf{thr}}}{m} + \dot{\boldsymbol{\omega}}^{\times}_k \underbrace{(\mathbf{r}_d - \mathbf{r}_c)}_{\mathbf{r}_{cd}} + \boldsymbol{\omega}^{\times}_k \boldsymbol{\omega}^{\times}_k (\mathbf{r}_d - \mathbf{r}_c) - \underbrace{\left(2 \cdot \boldsymbol{\omega}^{\times}_k \dot{\mathbf{r}}_c + \ddot{\mathbf{r}}_c\right)}_{\text{multi-body effects}} + \mathbf{b}_k + (\mathbf{v}_{\mathsf{ams}})_k \tag{46}$$

where m is the mass of the spacecraft, $\mathbf{f}_{\mathsf{thr}}$ is the sum of the body-fixed thrust-force, $\mathbf{r}_d$ is the location of the accelerometer in the body-frame, $\mathbf{r}_c$ is the location of the combined center-of-mass of the entire observatory, $\mathbf{b}$ is a vector of the accelerometer's intrinsic biases, and $\mathbf{v}_{\mathsf{ams}}$ is the measurement noise. For a discussion of the other potential measurement errors and their mitigation, see the reference[1].

A rigid-body assumption allows us to disregard center-of-mass motion ($\dot{\mathbf{r}}_c, \ddot{\mathbf{r}}_c = 0$), which results in

the accelerometer's measurement sensitivity matrix with respect to the attitude and rate error states as

$$H_{\text{ams}} \equiv \left[\frac{\partial \mathbf{h}_{\text{ams}}}{\partial(\delta\boldsymbol{\theta})} \quad \frac{\partial \mathbf{h}_{\text{ams}}}{\partial \boldsymbol{\omega}}\right]_{\hat{\mathbf{q}},\hat{\omega}} = \left[\mathbf{0}_{3\times 3} \quad \frac{\partial \mathbf{h}_{\text{ams}}}{\partial \boldsymbol{\omega}}\right]_{\hat{\mathbf{q}},\hat{\omega}} \tag{47}$$

The expression for the measurement partial with respect to $\boldsymbol{\omega}$ can be obtained from Eq. (46) using the *chain rule* and prudent cross product term-swapping.

$$\begin{aligned}\frac{\partial \mathbf{h}_{\text{ams}}}{\partial \boldsymbol{\omega}} &= \frac{\partial \dot{\boldsymbol{\omega}}^{\times}}{\partial \boldsymbol{\omega}}\mathbf{r}_{cd} + \frac{\partial \boldsymbol{\omega}^{\times}}{\partial \boldsymbol{\omega}}\boldsymbol{\omega}^{\times}\mathbf{r}_{cd} + \boldsymbol{\omega}^{\times}\frac{\partial \boldsymbol{\omega}^{\times}}{\partial \boldsymbol{\omega}}\mathbf{r}_{cd} + \boldsymbol{\omega}^{\times}\boldsymbol{\omega}^{\times}\frac{\partial \mathbf{r}_{cd}}{\partial \boldsymbol{\omega}} \qquad (48)\\ &= -\mathbf{r}_{cd}^{\times}\frac{\partial \dot{\boldsymbol{\omega}}}{\partial \boldsymbol{\omega}} - \left(\boldsymbol{\omega}^{\times}\mathbf{r}_{cd}\right)^{\times}\frac{\partial \boldsymbol{\omega}}{\partial \boldsymbol{\omega}} - \boldsymbol{\omega}^{\times}\mathbf{r}_{cd}^{\times}\frac{\partial \boldsymbol{\omega}}{\partial \boldsymbol{\omega}}\\ &= -\mathbf{r}_{cd}^{\times}\mathbf{I}^{-1}\left[(\mathbf{I}\boldsymbol{\omega})^{\times} - \boldsymbol{\omega}^{\times}\mathbf{I}\right] - \left(\boldsymbol{\omega}^{\times}\mathbf{r}_{cd}\right)^{\times} - \boldsymbol{\omega}^{\times}\mathbf{r}_{cd}^{\times}\\ &= -\mathbf{r}_{cd}^{\times}\mathbf{I}^{-1}\left[(\mathbf{I}\boldsymbol{\omega})^{\times} - \boldsymbol{\omega}^{\times}\mathbf{I}\right] - 2\boldsymbol{\omega}^{\times}\mathbf{r}_{cd}^{\times} + \mathbf{r}_{cd}^{\times}\boldsymbol{\omega}^{\times} \qquad (49)\end{aligned}$$

The preceding result was obtained using Eq. (18) and the identity $(\boldsymbol{a}^{\times}\mathbf{b})^{\times} = \boldsymbol{a}^{\times}\boldsymbol{b}^{\times} - \boldsymbol{b}^{\times}\boldsymbol{a}^{\times}$.

The covariance of the measurement noise can be derived from the AMS specification which asserts the root-mean-squared noise (a_{rms}) should be less than 8 μg_{rms} in the frequency range 0-10 Hz, and 80 μg_{rms} from 10-500 Hz. This implies that if a (single-sided) periodogram of acceleration-samples over a large time-interval was computed, its expected magnitude (A) over a given frequency range (e.g. Δf_{hz} = 10 Hz) should be less than

$$A_{0-10\,\text{hz}} \leq \frac{(a_{\text{rms}})^2}{\Delta f_{\text{hz}}} = \frac{8^2\,\mu g^2}{10\,\text{Hz}} = 6.4\,\frac{\mu g^2}{\text{Hz}} = 615.9\frac{\left(\frac{\mu\text{m}}{\text{s}^2}\right)^2}{\text{Hz}} \tag{50}$$

Figure 2 shows this is indeed the case for a sample taken from a non-maneuvering MMS-1. The AMS anti-alias filtering with break-point near 250 Hz can clearly be seen in the result. This implies a measurement covariance matrix with diagonal elements of $R \approx 3.8 \times 10^{-7}$ is reasonable, although the running sample-variance inside the AMS typically reads lower ($\bar{\sigma} \approx 16\,\mu g$) on most units.

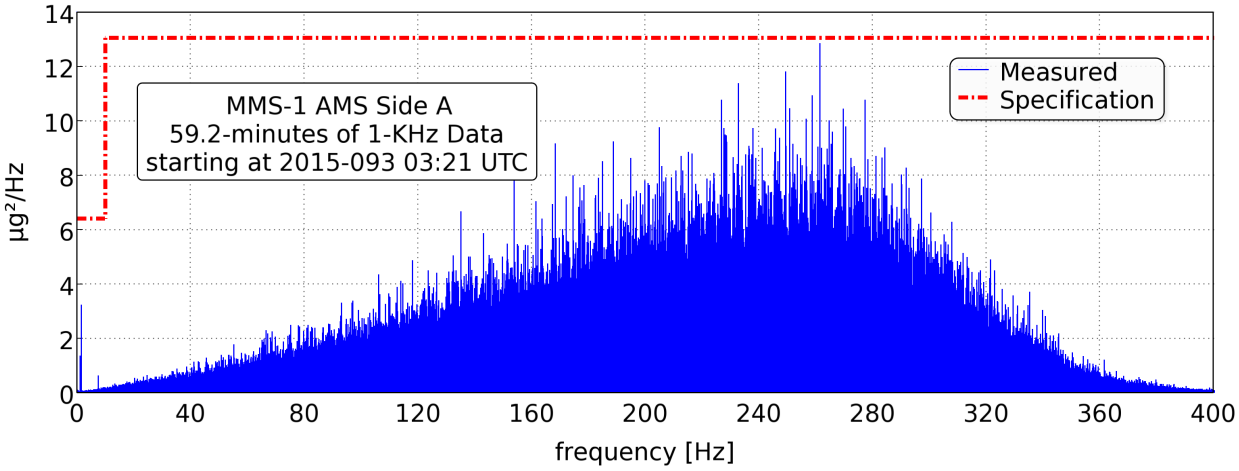

Figure 2. PSD of MMS-1 AMS 1 kHz Acceleration Data

2.2.3 Covariance Update

The final element associated with the receipt of new measurement observations, is the update of the error-state covariance P. For the MMS MEKF, *Jordan's form* of the update equation is used to improve numerical stability

$$P_k^+ = (\mathbb{I}_6 - K_k H_k) P_k^- (\mathbb{I}_6 - K_k H_k)^\mathsf{T} + K_k R_k K_k^\mathsf{T} \tag{51}$$

and the resultant is forced symmetric using averaging (of round-off errors)

$$P_k^+ = \frac{1}{2}\left(P_k^+ + \left(P_k^+\right)^\mathsf{T}\right) \tag{52}$$

To date, no stability problems have been experienced with the flight software MEKF that has operating continuously in single-precision floating-point for the past seven months.

2.3 Reset

Intrinsic to the MEKF is a process by which the information contained in the error states after a measurement $\boldsymbol{\delta}\mathbf{x}^+$ is transferred to the pre-update full state estimates $\mathbf{x}^-$, while "simultaneously" resetting the error state to zero. For the attitude state—using a Gibbs vector error parameterization—the reset operation looks like

$$\hat{\mathbf{q}}^+ = \boldsymbol{\delta}\mathbf{q}\left(\boldsymbol{\delta\theta}^+\right)^\otimes \hat{\mathbf{q}}^- \tag{53}$$

$$= \frac{1}{\sqrt{1+\|\boldsymbol{\delta\theta}^+\|^2}} \begin{bmatrix} \dfrac{\boldsymbol{\delta\theta}^+}{2} \\ 1 \end{bmatrix}^\otimes \hat{\mathbf{q}}^- \tag{54}$$

which is better performed as a two-step process

$$\hat{\mathbf{q}}^+_{\mathsf{unnorm}} = \begin{bmatrix} \dfrac{\boldsymbol{\delta\theta}^+}{2} \\ 1 \end{bmatrix}^\otimes \hat{\mathbf{q}}^- \tag{55}$$

followed by

$$\hat{\mathbf{q}}^+ = \frac{\hat{\mathbf{q}}^+_{\mathsf{unnorm}}}{\|\hat{\mathbf{q}}^+_{\mathsf{unnorm}}\|} \tag{56}$$

that effectively (and legitimately) enforces quaternion normalization. $\boldsymbol{\delta\theta}$ is now also set to zero, and (as shown in [4]) stays zero throughout propagation.

The reset of non-attitude states follow the standard linear addition update of an EKF. For example, the angular rate is updated by

$$\boldsymbol{\omega}^+ = \boldsymbol{\omega}^- + \boldsymbol{\delta\omega}^+ \tag{57}$$

and $\delta\boldsymbol{\omega}$ is set to zero. Because all of the reset/propagated error states are zero ($\delta\boldsymbol{\theta}^-$,$\delta\boldsymbol{\omega}^- = 0$), Eq. (34) collapses to simply

$$\begin{bmatrix} \delta\boldsymbol{\theta}_k^+ \\ \delta\boldsymbol{\omega}_k^+ \end{bmatrix} = \begin{bmatrix} K_{\theta_k} \\ K_{\omega_k} \end{bmatrix} \left[\mathbf{y}_k - \mathbf{h}\left(\hat{\mathbf{q}}_k^-, \hat{\boldsymbol{\omega}}_k^- \right) \right] \tag{58}$$

that—for what its worth—permits a so-called *implicit*[4] (i.e. combined) measurement/full-state update for the non-attitude state(s)

$$\boldsymbol{\omega}^+ = \boldsymbol{\omega}^- + K_{\omega_k} \left[\mathbf{y}_k - \mathbf{h}\left(\hat{\mathbf{q}}_k^-, \hat{\boldsymbol{\omega}}_k^- \right) \right] \tag{59}$$

effectively replacing Eqs. (34) and (57).

2.4 Propagation

Certain estimated quantites of the MEKF must be propagated from one measurement to the next. For the MMS ACS that propagation interval is typically the period of its 4 Hz control cycle, which is broken in to two sub-intervals—the center-of-integration time stamp of the star tracker measurements, and the arrival of the AMS packet (in order to transform and utilize the incremental velocity for closed-loop maneuvering). As previously mentioned, the nonlinear models expressed as ordinary differential equation in section 2.1 governing the full-state dynamics are propagated using a *Runge-Kutta* integrator. Due to the reset operation, the error-states are zero and do not need to be propagated. However, the covariance of the error-state vector does.

$$P_{k+1}^- = \Phi_k P_k \Phi_k^\mathsf{T} + Q_k \tag{60}$$

where $Q_k = E\left\{ \mathbf{w}_k \mathbf{w}_k^\mathsf{T} \right\}$. This is done discretely using the linearized error-state dynamical models derived in section 2.1 and summarized in Table 1. The linear system dynamics of the estimate

$$\delta\dot{\hat{\mathbf{x}}}(t) = F(t)\,\delta\hat{\mathbf{x}}(t) + G(t)\,\mathbf{w}(t) \tag{61}$$

are assumed constant over a small interval (Δt) so that the dynamics may be discretized as

$$\delta\hat{\mathbf{x}}_{k+1}^- = \Phi_k\,\delta\hat{\mathbf{x}}_k^+ + \mathbf{w}_k \tag{62}$$

and the derived state and noise-input *transition matrices* (Φ, Γ) may be used to propagate the error covariance. The most exact route to discretized the error-state dynamics is by using the method of Van Loan [10] with the *matrix exponential* applied to the following construction

$$A = \begin{bmatrix} -F & GWG^\mathsf{T} \\ \mathbf{0} & F^\mathsf{T} \end{bmatrix} \tag{63}$$

and then extracting the desired sub-matrices needed for the covariance propagation from

$$e^{A\Delta t} = \begin{bmatrix} B & \Phi_k^{-1} Q_k \\ \mathbf{0} & \Phi_k^\mathsf{T} \end{bmatrix} \tag{64}$$

For the flight software, it was entirely impractical to consider using the exponential to construct the necessary matrices in real-time. Instead, the ACS FSW resorted to the 1st-order approximation

$$\Phi_k \approx \mathbb{I}_6 + F(t_k)\,\Delta t \tag{65}$$

and also from [11]

$$Q_k = \int_0^{\Delta t} \Phi_k(\Delta t - \tau) W \Phi(\Delta t - \tau)^{\mathsf{T}} d\tau \tag{66}$$

where $W = \mathsf{diag}\{W_\theta, W_\omega\}$ is the diagonal matrix of spectral amplitudes (variances) for the "white" process-noise $\mathbf{w}(t)$ that drives the attitude and rate dynamics. Using the approximation for Φ from Eq. (65) yields,

$$Q_k \approx \begin{bmatrix} W_\theta \Delta t + \left(W_\theta \hat{\omega}_k^{\times} - \hat{\omega}_k^{\times} W_\theta\right)\frac{\Delta t^2}{2} + W_\omega \frac{\Delta t^3}{3} & W_\omega \frac{\Delta t^2}{2} + W_\omega F_\omega \frac{\Delta t^3}{3} \\ W_\omega \frac{\Delta t^2}{2} + F_\omega^{\mathsf{T}} W_\omega \frac{\Delta t^3}{3} & W_\omega \Delta t + \left(F_\omega W_\omega + W_\omega F_\omega^{\mathsf{T}}\right)\frac{\Delta t^2}{2} + F_\omega W_\omega F_\omega^{\mathsf{T}} \frac{\Delta t^3}{3} \end{bmatrix} \tag{67}$$

While the process noise is potentially very small, the MMS MEKF uses values around 10^{-6} to purposely "de-tune" the filter as protection against un-modeled dynamics, parameter errors, and maintain numerical stability. The matrix F_ω is the lower-right sub-matrix of $F(t)$, and is given by Eq. (19). Additionally, the ACS FSW propagation of Eq. (60) also made use of sparse-matrix multiplication optimizations to help reduce some of the MEKF computational load.

3 Augmented States for System Identification

In addition to the on-board filter that has been described, a more elaborate variant was developed for ground calibration. This *system-id MEKF* adds twelve states for mass property estimation, and three additional states to determine the steady-state force due to each thruster. The motivation for the work will now be described.

As a formation, the MMS mission must perform orbital maneuvers with an accuracy of roughly 1% (3σ) or else potentially fall in to a "tail-spin" of continuous orbit corrections. In order to satisfy this accuracy requirement, an AMS was added to each of the four observatories, and algorithms developed for velocity control using real-time feedback from the accelerometers[1]. By going "closed-loop", MMS successfully mitigated most of its parameter sensitivities (e.g. mass knowledge), while exposing itself to some others. Two system properties in particular were identified as the most potentially damaging while simultaneously the most difficult to estimate on the ground—the composite spacecraft center-of-mass (CM), and the steady-state thruster force.

The CM is important because knowledge of it's lever-arm to the accelerometer sensor-heads ($\mathbf{r}_{cd}$) is a key component of the centripetal-compensation algorithm used in the ACS for inertial velocity tracking. This compensation attempts to mitigate the velocity-errors that occur due to the second and third right-side terms of Eq. (46) when it is numerically integrated. Additionally, knowledge of the CM location is used (on the ground) to determine thruster duty-cycles that effectively balances thrusters into usable pure-translations (i.e. "torque-less") combinations.

The second-half of the "thrust-balancing" equation is the magnitude of the thrust itself. It was shown using Monte Carlo analysis, that steady-state thrust uncertainty of greater than $\pm 3\%$ (3σ) could result in an imbalance that would unacceptably degrade maneuvering performance and/or exceed stress limits on the structure (e.g. the ADP axial booms). It is important to note that accurate thrust-knowledge is actually needed due to secondary effects on the system, because closed-loop control has already eliminated it's primary effect. If that were not the case, a 3% error in thrust-knowledge would never permit a 1% maneuvering accuracy. Q.E.D.

Lastly, the second mass moments of inertia were added to the filter (reluctantly) when it appeared that the estimation processes simply would not perform well without them. Inertia mismatch between the MEKF model and the plant-truth aliased itself as errors in many other state estimates, and prevented the filter from achieving the desired degree of accuracy. The specific form in which it will be introduced—using the fuel's contribution as states, instead of using the entire observatory's mass properties directly—was also a just a progression of the design based on trial and error that departs from [12]. No claim is being made at this time that it represents a fundamental characteristic of an effective estimator, or even that it improves convergence, stability, etc. With this addition, the total augmented error-state vector (assuming a single thruster) has become

$$\delta\mathbf{x} = \begin{bmatrix} \delta\boldsymbol{\theta} & \delta\boldsymbol{\omega} & \delta\mathbf{b} & \delta\mathbf{r}_{\mathsf{f}} & \delta\mathbf{I}_{\mathsf{f}} & \delta \mathrm{f}_{ss} & \delta \mathrm{T}_{c} & \delta \mathrm{T}_{x} \end{bmatrix}^{\mathsf{T}} \tag{68}$$

3.1 Accelerometer Biases

In order to effectively estimate any of the system characteristics it is necessary to incorporate the accelerometer measurements. This can only be accomplished accurately if the accelerometers' intrinsic (thermo-electric) biases $\mathbf{b}_{(\mathsf{true})}$ are also estimated by the filter. The dynamics model for the biases is simply

$$\dot{\mathbf{b}} = \mathbf{f}_b(\mathbf{x}(t), \mathbf{w}(t)) = \mathbf{0} + \mathbf{w}_b(t) \tag{69}$$

since we assume the three axial biases are effectively constant over the relatively short calibration period ($\leq$ 2 hours), but could choose to set the process noise $\mathbf{w}_b$ to reflect a small bias drift—specified in the AMS to be less than 1 μg over 12-hours. The dynamic model is obviously identical for both the full-state dynamics ($\dot{\mathbf{b}}$) and the error states ($\delta\dot{\mathbf{b}}$), so the linearized error-state matrix expands to

$$F(t) = \begin{bmatrix} \dfrac{\partial \mathbf{f}_\theta}{\partial(\delta\boldsymbol{\theta})} & \dfrac{\partial \mathbf{f}_\theta}{\partial \boldsymbol{\omega}} & \dfrac{\partial \mathbf{f}_\theta}{\partial \mathbf{b}} \\ \dfrac{\partial \mathbf{f}_\omega}{\partial(\delta\boldsymbol{\theta})} & \dfrac{\partial \mathbf{f}_\omega}{\partial \boldsymbol{\omega}} & \dfrac{\partial \mathbf{f}_\omega}{\partial \mathbf{b}} \\ \dfrac{\partial \mathbf{f}_b}{\partial(\delta\boldsymbol{\theta})} & \dfrac{\partial \mathbf{f}_b}{\partial \boldsymbol{\omega}} & \dfrac{\partial \mathbf{f}_b}{\partial \mathbf{b}} \end{bmatrix} = \begin{bmatrix} \hat{\boldsymbol{\omega}}^{\times} & \mathbb{I}_3 & \mathbf{0}_{3\times 3} \\ \mathbf{0}_{3\times 3} & \mathbf{I}^{-1}\left[(\mathbf{I}\hat{\boldsymbol{\omega}})^{\times} - \hat{\boldsymbol{\omega}}^{\times}\mathbf{I}\right] & \mathbf{0}_{3\times 3} \\ \mathbf{0}_{3\times 3} & \mathbf{0}_{3\times 3} & \mathbf{0}_{3\times 3} \end{bmatrix} \tag{70}$$

For a measurement $\mathbf{y}_{\mathsf{ams}}$ taken by the accelerometer (Eq. (45)), the associated measurement sensitivity with respect to the bias is

$$\frac{\partial \mathbf{h}_{\mathsf{ams}}}{\partial \mathbf{b}} = \mathbb{I}_3 \tag{71}$$

3.2 Fuel Mass Perturbations

A careful bookkeeping and spin-balancing campaign[13] obtain what is believed to be very accurate knowledge of the stowed MMS observatories' dry mass properties. However, tests that practiced the loading and unloading of the 411.6-kg of fuel from the stiff elastomeric diaphragms inside the four semi-spherical tanks showed that the fuel-mass could take on a variety of "shapes" which could in turn cause significant perturbations in the total system mass properties[14].

Nine states need to be added to the filter in order to estimate the effect of the fuel mass property uncertainty—three for the location of the combined (in the four tanks) center-of-mass of the fuel $\mathbf{r}_{\mathsf{f}}$ in the body-frame, and six for the fuel-mass's moments and products of inertia about it's CM, $\mathbf{I}_{\mathsf{f}} = \begin{bmatrix} \mathrm{I}_{\mathsf{f}_{xx}} & \mathrm{I}_{\mathsf{f}_{yy}} & \mathrm{I}_{\mathsf{f}_{zz}} & \mathrm{I}_{\mathsf{f}_{xy}} & \mathrm{I}_{\mathsf{f}_{xz}} & \mathrm{I}_{\mathsf{f}_{yz}} \end{bmatrix}^{\mathsf{T}}$. Ground tests performed by Southwest Research Institute on a mock-up of a single MMS fuel tank, indicted that for a full tank, the mass participation in the fuel modes was relatively small ($\approx$18%) and at a frequency of around 5 Hz[15]. Since this was not expected to significantly affect the system dynamics (and high-fidelity simulation of the truth model verified it doesn't), the fuel state dynamics are also modeled as constants

$$\dot{\mathbf{r}}_{\mathsf{f}} = \mathbf{f}_r(\mathbf{x}(t), \mathbf{w}(t)) = \mathbf{0} + \mathbf{w}_r(t) \tag{72}$$

$$\dot{\mathbf{I}}_{\mathsf{f}} = \mathbf{f}_i(\mathbf{x}(t), \mathbf{w}(t)) = \mathbf{0} + \mathbf{w}_i(t) \tag{73}$$

The only non-zero partials in the linearized error-state dynamics are $\partial \mathbf{f}_\omega / \partial \mathbf{r}_{\mathsf{f}}$, and $\partial \mathbf{f}_\omega / \partial \mathbf{I}_{\mathsf{f}}$. Of the two, an analytic expression could only be found for the first. For the partial with respect to the "vectorized" fuel inertia, a numerical *finite-difference* solution was used to overcome the difficulties with taking partial derivative of a matrix with respect to a vector. While the finite-difference approach could also be brought to bear on the fuel center-of-mass partial derivative as well, the analytical solution is presented here because it is likely to be more computationally efficient, and because of the insights it can provide regarding the partitioning the system mass into dry and wet components.

The composite observatory center-of-mass, $\mathbf{r}_c$, can be broken down into wet and dry components

$$\mathbf{r}_c = \frac{m_{\mathsf{dry}}}{m} \mathbf{r}_{\mathsf{dry}} + \frac{m_{\mathsf{fuel}}}{m} \mathbf{r}_{\mathsf{f}} \tag{74}$$

where the total mass of the spacecraft $m = m_{\mathsf{fuel}} + m_{\mathsf{dry}}$, and $\mathbf{r}_{\mathsf{dry}}$ is the location of the dry-structure's center-of-mass in the body-frame. Utilizing a special case of the *parallel axis theorem*, the observatory's moment of inertia about it's center-of-mass, $\mathbf{I}$, can be expressed as a sum of its inertia about the body-frame origin, $\mathbf{J}$, and the "moment arm" from the origin to the center-of-mass ($\mathbf{r}_c$), and then broken down into the fuel's contribution and the dry-structure's contribution.

$$\begin{aligned} \mathbf{I} &= \mathbf{J} + m\mathbf{r}_c^{\times}\mathbf{r}_c^{\times} && (75) \\ &= \left(\mathbf{J}_{\mathsf{fuel}} + \mathbf{J}_{\mathsf{dry}}\right) + m\mathbf{r}_c^{\times}\mathbf{r}_c^{\times} \\ &= \left(\mathbf{I}_{\mathsf{fuel}} - m_{\mathsf{fuel}}\mathbf{r}_{\mathsf{f}}^{\times}\mathbf{r}_{\mathsf{f}}^{\times}\right) + \left(\mathbf{I}_{\mathsf{dry}} - m_{\mathsf{dry}}\mathbf{r}_{\mathsf{dry}}^{\times}\mathbf{r}_{\mathsf{dry}}^{\times}\right) + m\mathbf{r}_c^{\times}\mathbf{r}_c^{\times} && (76) \end{aligned}$$

Note that in the present notation, $\mathbf{I}_{\mathsf{fuel}}$ is a 3×3 matrix where as $\mathbf{I}_{\mathsf{f}}$ is a 6×1 vector. Proceeding with the derivation, Eq. (74) is combined with Eq. (76) to yield an expression for the spacecraft's

moment of inertia as an explicit function of the new state $\mathbf{r}_\mathsf{f}$

$$\mathbf{I} = \mathbf{I}_{\mathsf{fuel}} + \mathbf{I}_{\mathsf{dry}} + m_{\mathsf{dry}} \left(\tfrac{m_{\mathsf{dry}}}{m} - 1\right) \mathbf{r}_{\mathsf{dry}}^{\times} \mathbf{r}_{\mathsf{dry}}^{\times} + m_{\mathsf{fuel}} \left(\tfrac{m_{\mathsf{fuel}}}{m} - 1\right) \mathbf{r}_{\mathsf{f}}^{\times} \mathbf{r}_{\mathsf{f}}^{\times} + \tfrac{m_{\mathsf{dry}} \cdot m_{\mathsf{fuel}}}{m} \left(\mathbf{r}_{\mathsf{f}}^{\times} \mathbf{r}_{\mathsf{dry}}^{\times} - \mathbf{r}_{\mathsf{f}}^{\times} \mathbf{r}_{\mathsf{dry}}^{\times}\right) \quad (77)$$

Using an alternate form of the angular rate dynamics with the control-torque shown as a cross product of the thrust-force, and then taking its partial derivative with respect to the fuel CM yields

$$\mathbf{I}\dot{\boldsymbol{\omega}} + \boldsymbol{\omega}^{\times} \mathbf{I}\boldsymbol{\omega} = (\mathbf{r}_{\mathsf{thr}} - \mathbf{r}_c)^{\times} \mathbf{f}_{\mathsf{thr}} \quad (78)$$

$$\mathbf{I}\frac{\partial \dot{\boldsymbol{\omega}}}{\partial \mathbf{r}_\mathsf{f}} + \frac{\partial \mathbf{I}}{\partial \mathbf{r}_\mathsf{f}} \dot{\boldsymbol{\omega}} + \boldsymbol{\omega}^{\times} \frac{\partial \mathbf{I}}{\partial \mathbf{r}_\mathsf{f}} \boldsymbol{\omega} = \mathbf{f}_{\mathsf{thr}}^{\times} \frac{\partial \mathbf{r}_c}{\partial \mathbf{r}_\mathsf{f}}$$

$$\frac{\partial \dot{\boldsymbol{\omega}}}{\partial \mathbf{r}_\mathsf{f}} = \mathbf{I}^{-1} \left[\mathbf{f}_{\mathsf{thr}}^{\times} \frac{\partial \mathbf{r}_c}{\partial \mathbf{r}_\mathsf{f}} - \frac{\partial \mathbf{I}\dot{\boldsymbol{\omega}}}{\partial \mathbf{r}_\mathsf{f}} - \boldsymbol{\omega}^{\times} \frac{\partial \mathbf{I}\boldsymbol{\omega}}{\partial \mathbf{r}_\mathsf{f}}\right] \quad (79)$$

The terms needed to evaluate Eq. (79) can be determined by taking the partial derivatives of Eqs. (74) and (77). Specifically, they are

$$\frac{\partial \mathbf{r}_c}{\partial \mathbf{r}_\mathsf{f}} = \frac{m_{\mathsf{fuel}}}{m} \mathbb{I}_3 \quad (80)$$

and

$$\frac{\partial \mathbf{I}\boldsymbol{\omega}}{\partial \mathbf{r}_\mathsf{f}} = m_{\mathsf{fuel}} \left(1 - \frac{m_{\mathsf{fuel}}}{m}\right) \left[\left(\mathbf{r}_{\mathsf{f}}^{\times} \boldsymbol{\omega}\right)^{\times} + \mathbf{r}_{\mathsf{f}}^{\times} \boldsymbol{\omega}^{\times}\right] - \frac{m_{\mathsf{fuel}}\, m_{\mathsf{dry}}}{m} \left[\left(\mathbf{r}_{\mathsf{dry}}^{\times} \boldsymbol{\omega}\right)^{\times} + \mathbf{r}_{\mathsf{dry}}^{\times} \boldsymbol{\omega}^{\times}\right] \quad (81)$$

The final required quantity, $\partial \mathbf{I}\dot{\boldsymbol{\omega}} / \partial \mathbf{r}_\mathsf{f}$, is obtained by directly swapping $\boldsymbol{\omega}$ with $\dot{\boldsymbol{\omega}}$ everywhere it appears in Eq. (81), and then estimating $\dot{\hat{\boldsymbol{\omega}}}$ using the expected values of Eqs. (78) and (74) (i.e. by substituting in the current state estimates in place of truth-states in *Euler's equation*).

The acceleration measurement sensitivities associated with the new states are

$$\frac{\partial \mathbf{h}_{\mathsf{ams}}}{\partial \mathbf{r}_\mathsf{f}} = -\mathbf{r}_{cd}^{\times} \frac{\partial \dot{\boldsymbol{\omega}}}{\partial \mathbf{r}_\mathsf{f}} - \left(\dot{\boldsymbol{\omega}}^{\times} + \boldsymbol{\omega}^{\times} \boldsymbol{\omega}^{\times}\right) \frac{\partial \mathbf{r}_c}{\partial \mathbf{r}_\mathsf{f}} \quad (82)$$

$$\frac{\partial \mathbf{h}_{\mathsf{ams}}}{\partial \mathbf{I}_\mathsf{f}} = -\mathbf{r}_{cd}^{\times} \frac{\partial \dot{\boldsymbol{\omega}}}{\partial \mathbf{I}_\mathsf{f}} \quad (83)$$

which may be evaluated using the results already calculated for Eq. (79), and the aforementioned finite-difference result for the fuel-inertial partials.

3.3 Thruster Dynamics

The most difficult part of estimating the thruster output was due to "warm-up" effects. Based on ground-test data, it is expected that the MMS thrusters take nearly 15-seconds to reach true steady-state operation. It was unreasonable to expect that a single-thruster-at-a-time calibration (recall, the goal is the individual thruster modulation duty-cycles) could accommodate such a long period of "wasted" un-balanced thrust as part of its process. Instead, the data from the thruster delta-qualification program was mined in order to construct a dynamic model of the warm-up effect.

The result was a heuristic two-node thermal model, combined with a polynomial fit of the classical thrust-coefficient. The two thermal states along with a state representing the steady-state force itself, adds at least three states to the MEKF (but potentially three per thruster, depending on how the designer chooses to handle the individual thruster calibration in the filter software).

The first component of the new model is a two node/state thermal model that approximates the heating and cooling of the thrust-chamber (where the catalyst-bed sits and two-stage hydrazine decomposition occurs). A two-node model was selected after the observation that there was no single cooling decay-constant capable of fitting the data "well". The only elements of the models that are known from first-principles are: the flame-temperature of the hydrazine reaction ($T_{\text{flame}} = 1875^{\circ}F$ [1024 C]), and the cooling is either conductive/convective (linear in temperature) or radiative (quartic in temperature). A schematic of the model is shown in Fig. 3.

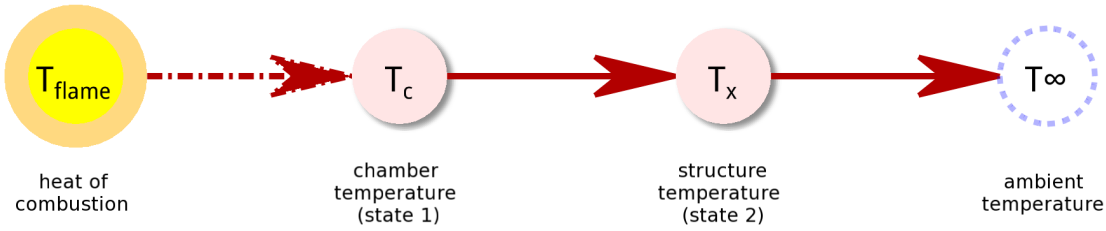

Figure 3. Thruster Thermal Node Model

The full nonlinear (process) dynamic models for the two new thermal states are

$$\dot{T}_c = \mathrm{f}_{tc}(\mathbf{x}(t), \mathbf{u}(t), \mathbf{w}(t)) = u(t) \cdot k_{\mathrm{f}} \left(T_{\text{flame}} - T_c\right) + k_x \left(T_x - T_c\right) + w_{tc}(t) \tag{84}$$

$$\dot{T}_x = \mathrm{f}_{tx}(\mathbf{x}(t), \mathbf{u}(t), \mathbf{w}(t)) = \underbrace{k_x \left(T_c - T_x\right) + k_\infty \left(T_\infty - T_x\right)}_{\text{conductive}} + \underbrace{k_r \left(T_\infty^4 - T_x^4\right)}_{\text{radiative}} + \underbrace{w_{tx}(t)}_{\text{noise}} \tag{85}$$

where $u(t)$ is the control input (binary valve open-close status) for a particular thruster, and k_{f}, k_x, and k_r are constant coefficients that were "hand-tuned" to fit the MMS qualification data (and later the flight data). The magnitude of thrust-force produced (f_{thr}) is found using a 3rd-order polynomial fit (p_0, p_1, p_2, p_3) of the chamber temperature-state multiplied by the third state to be added to the filter—the steady-state force magnitude (f_{ss})

$$f_{\text{thr}}(t) = \left[p_3 T_c^3(t) + p_2 T_c^2(t) + p_1 T_c(t) + p_0\right] f_{ss} \tag{86}$$

The thrust-vector—as used in Eq. (78)—is found by multiplying the magnitude by a unit-vector in the direction the thruster's nozzle is pointing ($\mathbf{d}_{\text{thr}}$), and regulating the output with the (binary) control input signal, $u(t)$. In equation form, the preceding statement may be written as

$$\mathbf{f}_{\text{thr}}(t) = f_{\text{thr}}(t) \cdot \mathbf{d}_{\text{thr}} \cdot u(t) \tag{87}$$

where the polynomials coefficients (p_n's) were again derived from the MMS qualification data—as was the somewhat arbitrary decisions to use a 3rd-order fit.

Lastly, the true parameter of interest, the steady-state thrust-force f_{ss}, is a function only of the hydrazine inlet-pressure in the propulsion system. Over the calibration period (e.g. a few short

thruster-pulses), this value is assumed to be constant. As has already been well established, the dynamic model of a constant, driven by process noise, is

$$\dot{f}_{ss} = f_{ss}(\mathbf{x}(t), \mathbf{w}(t)) = 0 + w_{fss}(t) \tag{88}$$

The effectiveness of this model in matching the qualification-test data is evidenced in Fig. 4 by how well dashed green line representing the simulated chamber temperature state (T_c sim) tracks the blue line of measured chamber temperature data (T_c meas), as well as the normalized force curves (black dashed-line vs. red measurement-dots) for a pulse-train of three consecutive valve cycles each continuously expelling 3.3-second of fuel on a 20-seconds interval (taken from a non-pulsed-width-modulated/class-A-pulse data set for the radial thrusters).

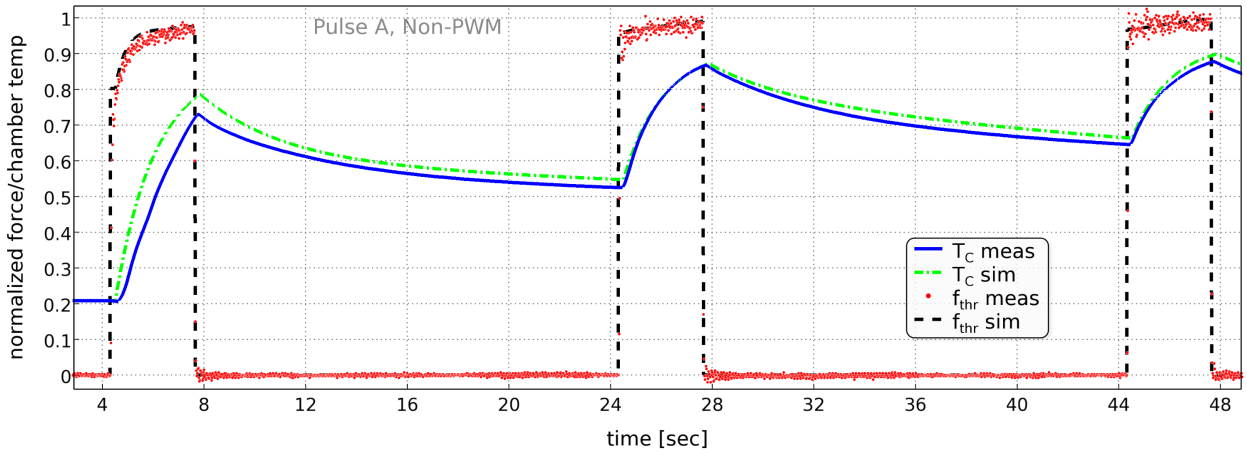

Figure 4. Comparison of Simulated vs. Measured Temperatures and Forces

The non-zero partial derivatives for the three new thruster-states, for use in the linearized error-state dynamics matrix $F(t)$, are

$$\left.\frac{\partial \mathbf{f}_{\omega}}{\partial T_c}\right|_{\hat{\mathbf{x}},\mathbf{u}} = \hat{\mathbf{I}}^{-1}\left[(\mathbf{r}_{\text{thr}} - \hat{\mathbf{r}}_c)^{\times}\,\mathbf{d}_{\text{thr}} \cdot u(t) \cdot \left.\frac{\partial f_{\text{thr}}}{\partial T_c}\right|_{\hat{\mathbf{x}},\mathbf{u}}\right] \tag{89}$$

$$\left.\frac{\partial \mathbf{f}_{\omega}}{\partial f_{ss}}\right|_{\hat{\mathbf{x}},\mathbf{u}} = \hat{\mathbf{I}}^{-1}\left[(\mathbf{r}_{\text{thr}} - \hat{\mathbf{r}}_c)^{\times}\,\mathbf{d}_{\text{thr}} \cdot u(t) \cdot \left.\frac{\partial f_{\text{thr}}}{\partial f_{ss}}\right|_{\hat{\mathbf{x}},\mathbf{u}}\right] \tag{90}$$

$$\left.\frac{\partial \mathbf{f}_{tc}}{\partial T_c}\right|_{\hat{\mathbf{x}},\mathbf{u}} = -k_{\mathsf{f}} \cdot u(t) - k_x \tag{91}$$

$$\left.\frac{\partial \mathbf{f}_{tc}}{\partial T_x}\right|_{\hat{\mathbf{x}},\mathbf{u}} = k_x \tag{92}$$

$$\left.\frac{\partial \mathbf{f}_{tx}}{\partial T_c}\right|_{\hat{\mathbf{x}},\mathbf{u}} = k_x \tag{93}$$

$$\left.\frac{\partial \mathbf{f}_{tx}}{\partial T_x}\right|_{\hat{\mathbf{x}},\mathbf{u}} = -k_x - k_\infty - 4k_r\hat{T}_x^3 \tag{94}$$

The partial derivatives of the steady-state thrust force with respect to the thermal-states needed to complete the evaluation Eqs. (89) and (90) are

$$\left.\frac{\partial f_{\mathsf{thr}}}{\partial T_c}\right|_{\hat{\mathbf{x}},\mathbf{u}} = \left[3\,p_3\,\hat{T}_c(t)^2 + 2\,p_2\,\hat{T}_c(t) + p_1\right]\cdot \hat{f}_{ss} \tag{95}$$

$$\left.\frac{\partial f_{\mathsf{thr}}}{\partial f_{ss}}\right|_{\hat{\mathbf{x}},\mathbf{u}} = p_3\,\hat{T}_c^3(t) + p_2\,\hat{T}_c^2(t) + p_1\,\hat{T}_c(t) + p_0 \tag{96}$$

The non-zero measurement sensitivity partial derivatives with respect to the new thruster-states are, for the accelerometer measurement equation

$$\left.\frac{\partial \mathbf{h}_{\mathsf{ams}}}{\partial f_{ss}}\right|_{\hat{\mathbf{x}},\mathbf{u}} = \left[\frac{1}{m}\mathbf{d}_{\mathsf{thr}} - \hat{\mathbf{r}}_{cd}^{\times}\hat{\mathbf{I}}^{-1}\left(\mathbf{r}_{\mathsf{thr}} - \hat{\mathbf{r}}_c\right)^{\times}\mathbf{d}_{\mathsf{thr}}\right]\cdot u(t)\cdot \left.\frac{\partial f_{\mathsf{thr}}}{\partial f_{ss}}\right|_{\hat{\mathbf{x}},\mathbf{u}} \tag{97}$$

$$\left.\frac{\partial \mathbf{h}_{\mathsf{ams}}}{\partial T_c}\right|_{\hat{\mathbf{x}},\mathbf{u}} = \left[\frac{1}{m}\mathbf{d}_{\mathsf{thr}} - \hat{\mathbf{r}}_{cd}^{\times}\hat{\mathbf{I}}^{-1}\left(\mathbf{r}_{\mathsf{thr}} - \hat{\mathbf{r}}_c\right)^{\times}\mathbf{d}_{\mathsf{thr}}\right]\cdot u(t)\cdot \left.\frac{\partial f_{\mathsf{thr}}}{\partial T_c}\right|_{\hat{\mathbf{x}},\mathbf{u}} \tag{98}$$

where the trailing terms—the thrust-force magnitude partials—are once again obtained by using Eqs. (95) and (96).

4 Filter Performance

Having defined the structure of both the ACS flight software MEKF and an augmented-state version for ground calibration, we now turn our attention to a battery of performance results for each. The two sources available by which to gauge performance are the MMS high-fidelity, nonlinear, time-domain simulation constructed in GSFC's *Freespace Simulation Environment*[16], and ground-processing of telemetered flight data from the observatories.

4.1 Smoothing

Before launching in to the performance result, one small aside is also worth mentioning. In order to access the true performance of the methods—and especially to obtain a definitive attitude and rate solution from the flight telemetry for which "truth" is not available—a *Rauch-Tung-Stribel* (RTS) optimal batch smoother was applied to the filtered results[17]. The RTS smoother falls in to the category of *fixed-interval smoothers*, and although it does not improve the final state-estimates from a filter operating on a finite sequence of data, it can significantly improve the estimates internal to the interval.

The algorithm for the discrete-time RTS smoother uses stored values for $\hat{\mathbf{x}}_k^-$, $\hat{\mathbf{x}}_k^+$, Φ_k, P_k^-, and P_k^+ from the forward-time MEKF to sweep backwards through the data and improve the estimates and error-covariance. The smoother initializes it's recursion with the final (N-th) forward time estimates of the MEKF, $\hat{\mathbf{x}}_{\mathsf{sm}_N} = \hat{\mathbf{x}}_N^+$ and $P_{\mathsf{sm}_N} = P_N^+$, and proceeds (backwards in k) in the following manner[6]

$$K_{\mathsf{sm}_k} \equiv P_k^+\Phi_k^{\mathbf{T}}\left(P_{k+1}^-\right)^{-1} \tag{99}$$

$$\hat{\mathbf{x}}_{\mathsf{sm}_k} = \hat{\mathbf{x}}_k^+ + K_{\mathsf{sm}_k}\left(\hat{\mathbf{x}}_{\mathsf{sm}_{k+1}} - \hat{\mathbf{x}}_{k+1}^-\right) \tag{100}$$

$$P_{\mathsf{sm}_k} = P_k^+ - K_{\mathsf{sm}_k}\left(P_{k+1}^- - P_{\mathsf{sm}_{k+1}}\right)K_{\mathsf{sm}_k}^{\mathsf{T}} \tag{101}$$

The only downside to using the fixed-interval smoother is the burden of matrix storage, the fact that is it only possible as batch process, and that it does not improve the final estimate (for system identification). Nevertheless, many of the subsequent plots of the key system parameters-of-interest will also show an annotated curve for the smoothed estimates.

4.2 Attitude and Rate Determination Performance

4.2.1 Simulation

A set of comparative plots shows the MEKF attitude and rate estimates surrounding a single 2.5-second pulse from MMS thruster #1. This unit is radially directed in the observatory's minus-y direction (i.e. it applies a +y force), and is located approximately 0.5-meters below the CM. A "4-lb" thruster, at beginning-of-life pressure, applies 19.8 N of steady-state thrust. The mini-maneuver induces approximately 2.5° of nutation, and roughly the same amount of precession in the spacecraft's total angular momentum. Figure 5 shows the effect of the single-thruster pulse on the observatory's angular rate, as well as the 1 kHz acceleration at the sensor heads.

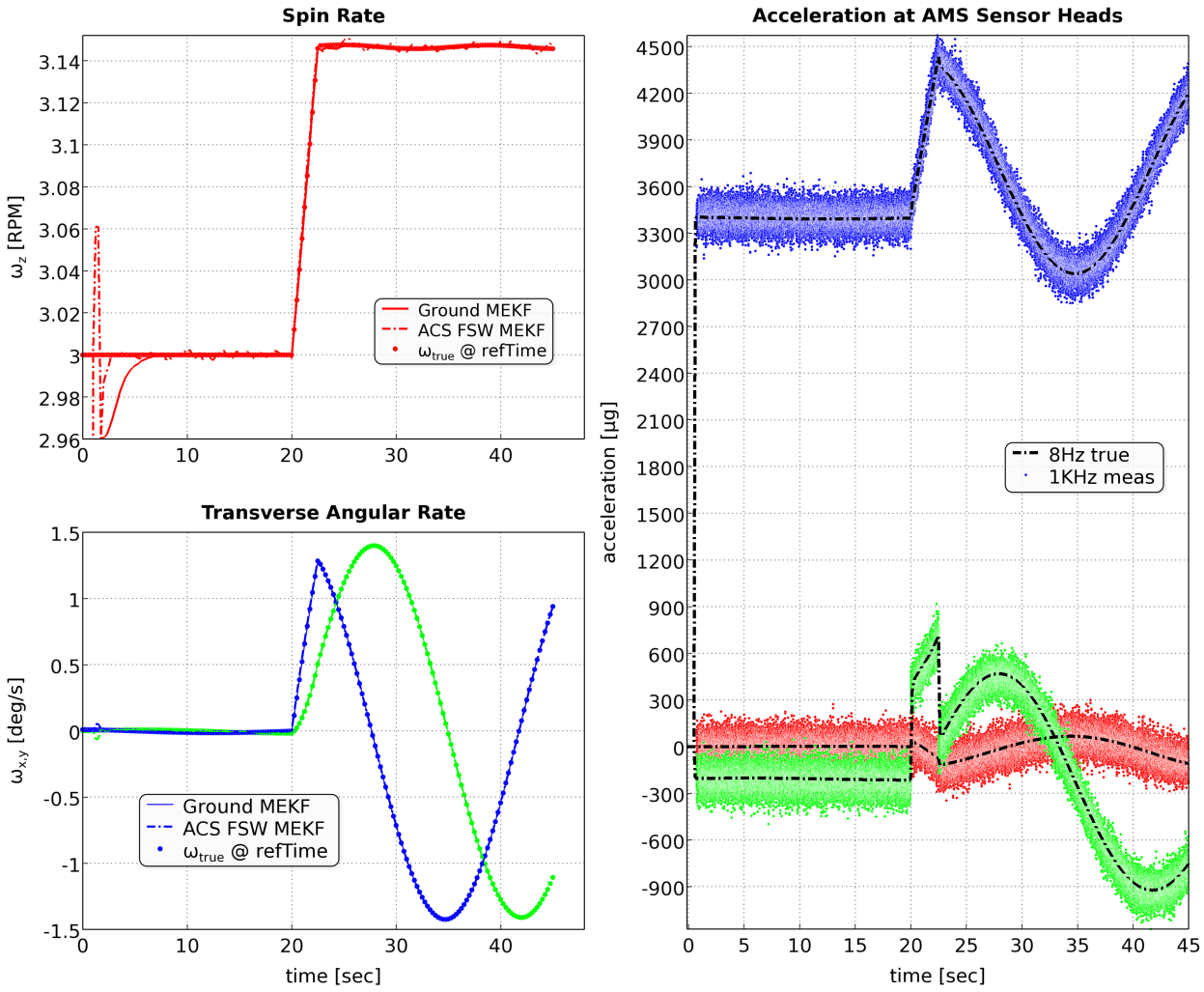

Figure 5. Simulated Single-Pulse Maneuver

The next series of plots show—for the same simulation set-up as above—the attitude and rate errors of the various estimators developed in the preceding sections. It is clear from Fig. 6 that the off-line MEKF outperforms the flight implementation, and unsurprisingly that the RTS smoother (applied to the augmented-state filter) outperforms both.

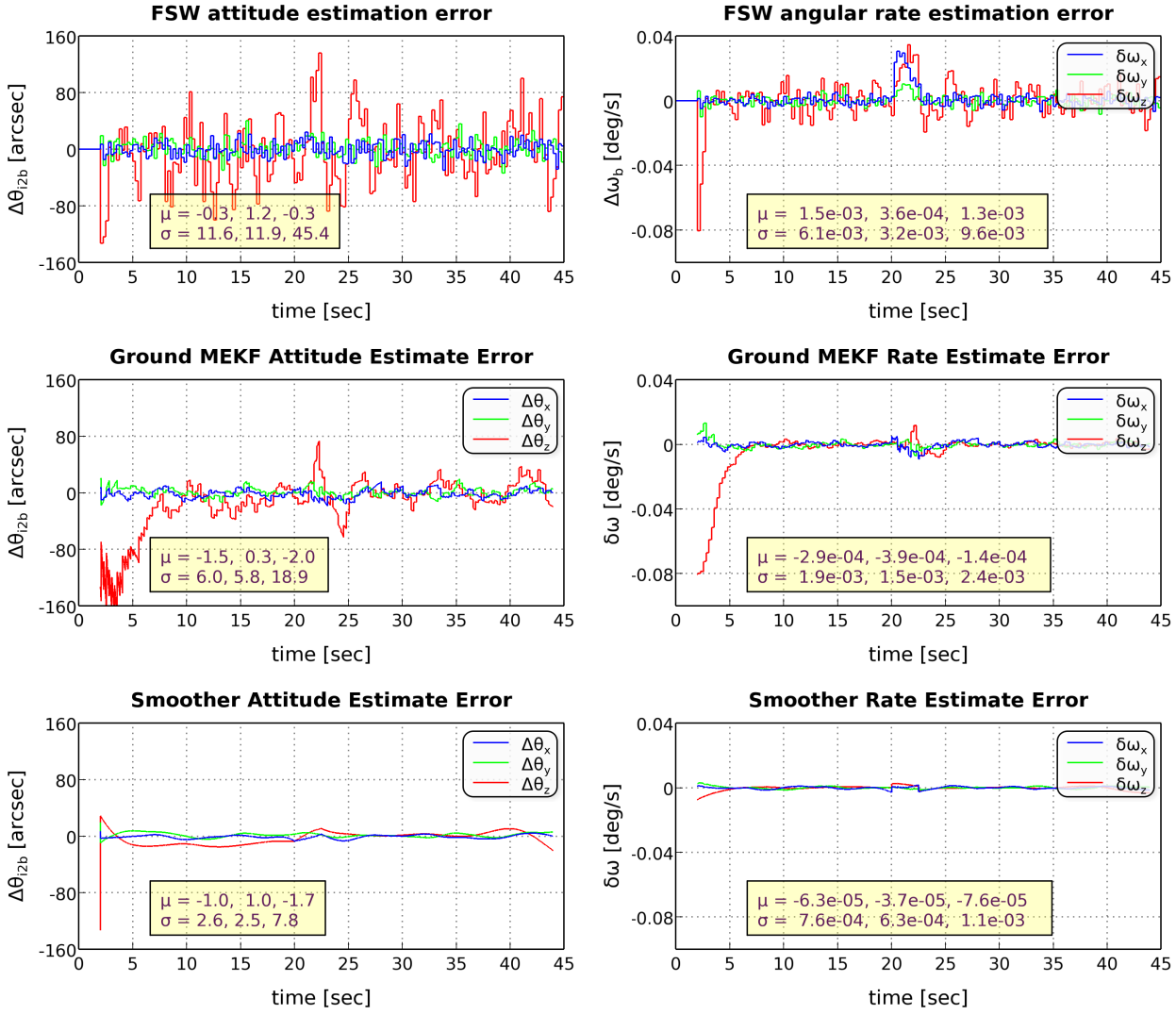

Figure 6. Comparison of Filtered Attitude and Rate Estimates of Simulated Maneuver

There are a number of reasons why the higher-order filter produces a more accurate result. First, it is interesting to note that the augmented-state MEKF will—with identical tuning of the process and measurement noise statistics—very closely match the results of the six-state (flight software) MEKF as long as the acceleration measurements are excluded. Recall that the FSW MEKF was de-tuned as protection against un-modeled dynamics and numerical instability. With the acceleration measurements utilized by a filter with elevated attitude and rate process noise—while using an optimal measurement noise covariance—the relatively noisy AMS observations "drag the rate estimate about" too heavily. Either of two solutions will suffice to fix the issue—increase the noise statistics of the acceleration measurements, or (preferably) reduce the rate-dynamics process noise covariance. If either of these rectifications are applied, the results shown in Fig. 6 are achievable.

4.2.2 Flight Telemetry

Figure 7 shows recorded telemetry from the ACS during a calibration maneuver performed on the observatory designated MMS1 that took place on April 1, 2015 03:12 (UTC). This maneuver (EA019) occurred while the observatories were in a semi-stowed state—only the ADP receiving element and the magnetometer booms were deployed. It was designed with the goal of exercising each individual thruster in matched pulses that induced—and then canceled—nutation. This was accomplished by spacing the 2.5-sec firings one-half of a nutation period apart (≈15-sec). A couple of thrusters were fired four times in series to provide a more extended view of warm-up effects. Spin-rate change was essential for system-identification purposes—since it potentially separates the accelerometer-biases (static) from center-of-mass offset knowledge errors (a function of rate). Care was taken not to exceed the star tracker's transverse or spin-rate limits, induce excessive pointing error (a thermal constraint), or significantly perturb the orbit (a collision risk). Nevertheless, it still made for a wild ride!

These initial plots of the telemetry focus in on the first pulse in the maneuver. The telemetered data compares favorably with the simulation result shown in Fig. 5. The most glaring difference

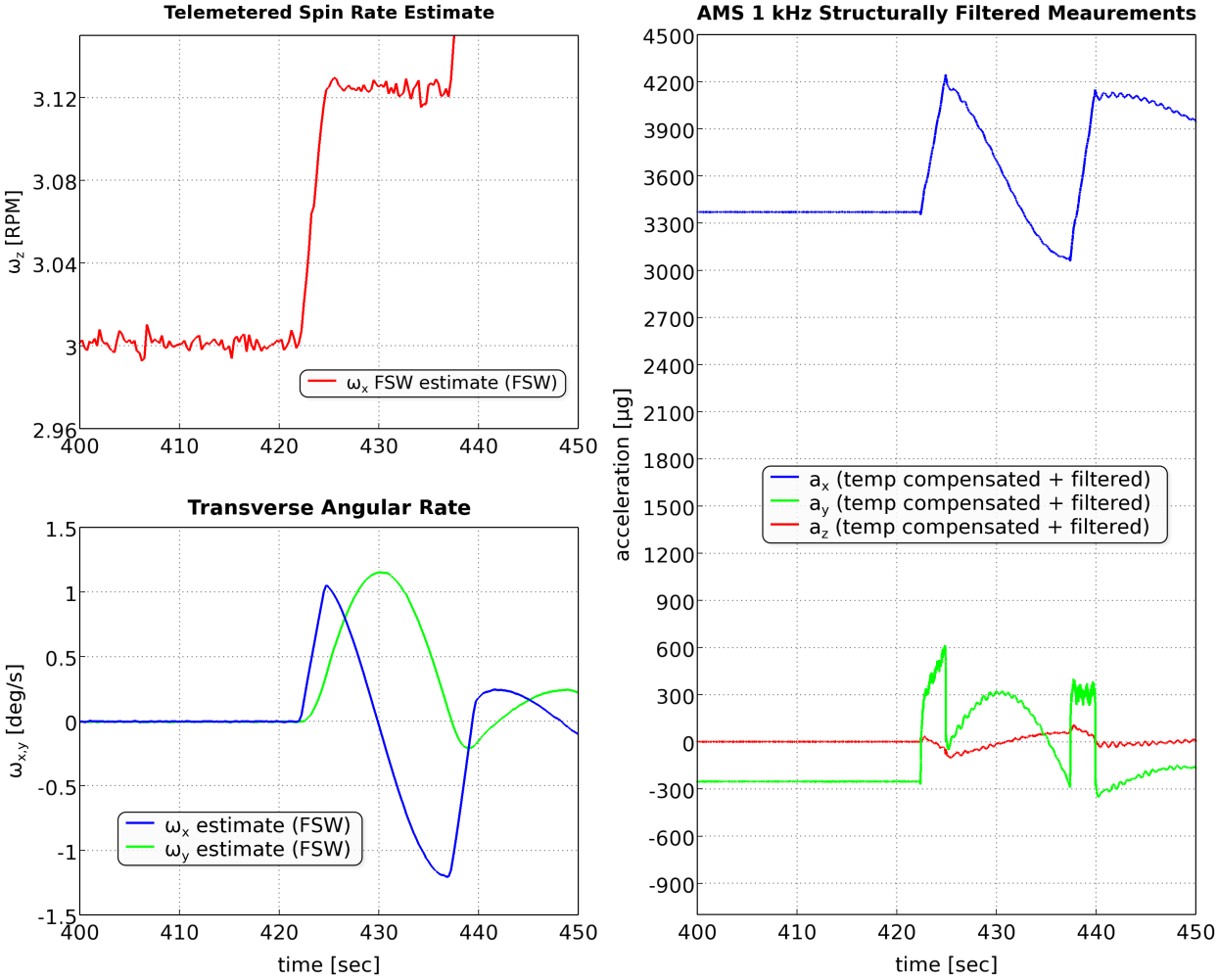

Figure 7. ACS Flight Software Telemetry from the Start of the EA019 Maneuver

between the two is the acceleration plots on the right—the flight data is noticeably smoother. The reason behind this is that the raw-burst data from the AMS has undergone two operations in order to make it presentable—a temperature correction, and a structural (low-pass) filter. While the first is fairly benign, the structural filter eliminates almost all of the high-frequency noise characteristics of the AMS measurements. Unfortunately, this pre-processing step is needed because otherwise the effective rigid-body response is completely swamped by the excited structural modes. A high-order Finite-Impulse-Response filter with "brick-wall" frequency cut-off near 25 Hz was used because the linear phase-distortion (i.e. fixed sample lag) that it introduces is trivial to undo.

A good metric for the performance of the flight MEKF is the measurement residuals for each of the star tracker's camera head units (CHU)—shown in Fig. 8. They indicate that the ACS MEKF

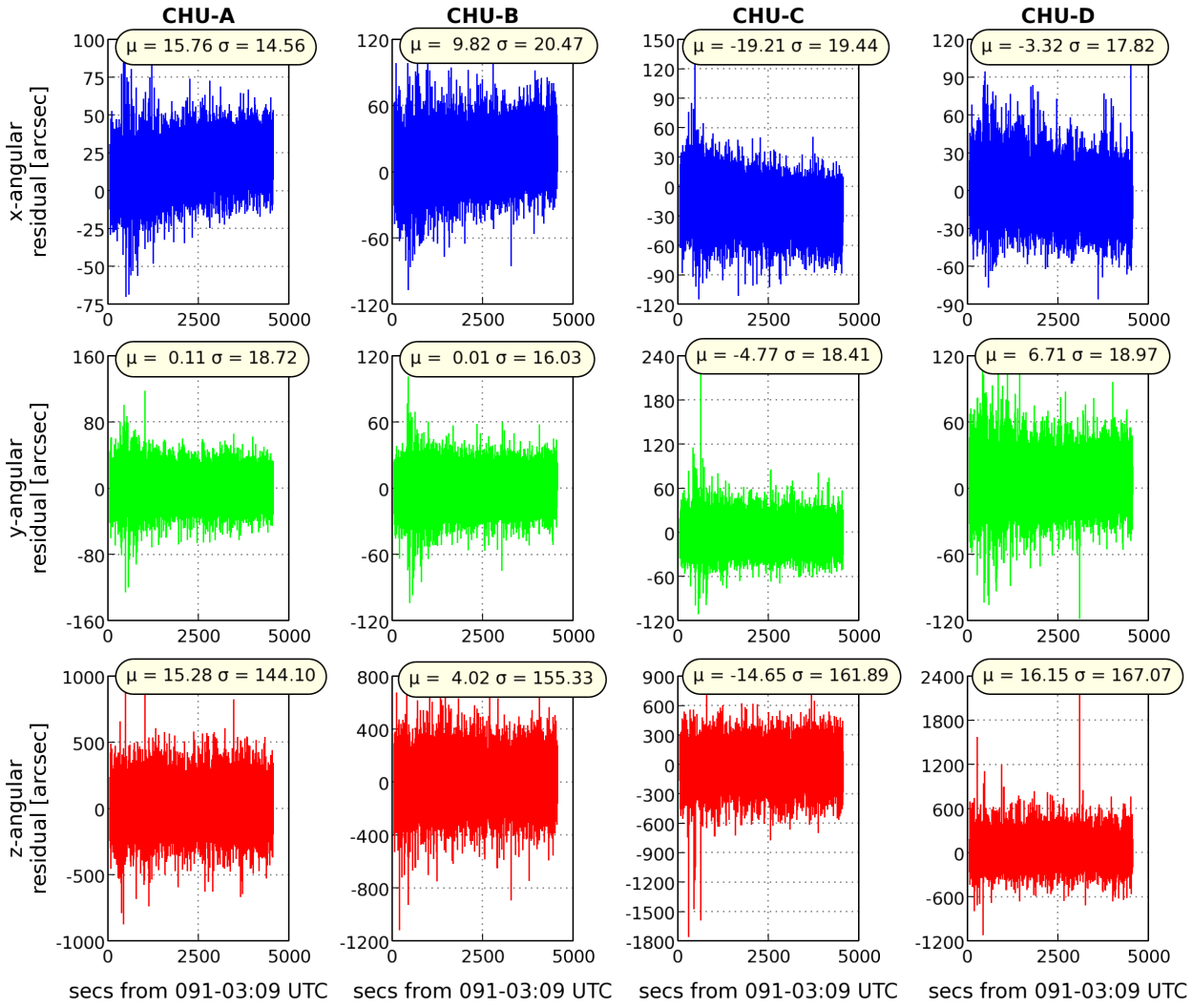

Figure 8. ACS MEKF CHU Measurement Residuals During EA019 Maneuver

is well-behaved—despite the aggressive maneuvering—and that the measurements are reasonably unbiased due to successful star sensor alignment calibration campaign[8]. Unfortunately, the statistics also show that the z-axis (bore-site) residual seems to be larger than expected. At roughly 170 arcsec (1σ), the STS solution error is at nearly three times the spec-level of 60 arcsec (1σ). It

has been independently verified[8] that these elevated noise-levels about the bore-site persist during coasting—confirming that the phenomena is not an artifact of the ACS MEKF design, and most likely are just intrinsic to the tracker measurements themselves.

4.3 Mass Property and Thrust Estimation Performance

The effectiveness of the augmented-state MEKF at estimating the MMS mass properties and steady-state thrust magnitude for will now be demonstrated. As has already been asserted, the system-id filter performs nearly identical to the FSW MEKF when fed only star sensor measurements, and de-tuned to an equivalent degree. Despite have a significantly larger number of states, the system-id MEKF remains stable and converges in a reasonable vicinity of the true plant parameters. It also is well-behaved when given acceleration measurements at any interval between 0-1000 Hz. Despite the author's concerns during the state-augmentation process, there appeared to be no serious *information dilution* pitfalls.

One caveat regarding the augmented filter's performance at estimating thrust is a sensitivity to correct timing of the control input, $u(t)$. If the valve opening and closing times are not well known, or there is significant transport lag, the filter will tend to underestimate the thrust-level and/or over estimate the inertia. This touches upon one of the two coupled (aliasing) problems for MMS system identification. The thrust/inertia ambiguity is the first, and the center-of-mass/bias equivalency is another. Only through sufficient variance of excitation (i.e. spin-rate, nutation, thrust) can these quantities be resolved. Examination of the complete linearized measurement matrix $H(t)$

$$(H_{\mathsf{ams}})_k = \left[\mathbf{0}_{3\times 3} \quad \frac{\partial \mathbf{h}_{\mathsf{ams}}}{\partial \boldsymbol{\omega}} \quad \mathbb{I}_3 \quad \frac{\partial \mathbf{h}_{\mathsf{ams}}}{\partial \mathbf{r}_{\mathsf{f}}} \quad \frac{\partial \mathbf{h}_{\mathsf{ams}}}{\partial \mathbf{I}_{\mathsf{f}}} \quad \frac{\partial \mathbf{h}_{\mathsf{ams}}}{\partial \mathrm{f}_{ss}} \quad \frac{\partial \mathbf{h}_{\mathsf{ams}}}{\partial \mathrm{T}_c} \quad \mathbf{0}_{3\times 3} \right]_{\hat{\mathbf{x}}_k} \tag{102}$$

might offer some additional insight as to the observability of the augmented error-states (and which states need to be excited), but that analytical effort has not been pursued. Instead, evidence of the filter's efficacy will be shown by way of simulation and Monte Carlo analysis.

4.3.1 Simulation

A computer simulation was performed that utilized a pair of thruster-pulses to perturb the spacecraft in a manner similar to the single-pulse of section 4.2.1. As part of the system-id post-processing, the errors listed in Table 2 in the initial estimates of the augmented (quasi-constant) states were introduced to demonstrate performance.

Table 2. Summary of Initial Estimate Errors

Parameter	Error
accelerometer biases	+20 μg
fuel center-of-mass	+50 mm
fuel moments of inertia	+10 kg-m^2
steady-state thrust magnitude	+5%

The process noise variances (i.e. the diagonal elements of the W matrix) were selected to be 10^{-16} for the bias ($\mathbf{b}$) and fuel states ($\mathbf{r}_{\mathsf{f}}$, $\mathbf{I}_{\mathsf{f}}$). The variances of the thruster-related states (f_ss, T_c, T_x) were set larger (at 10^{-9}) to account for model uncertainty. The results of the estimation process with 4 Hz star sensor measurements, and 100 Hz (decimated) acceleration samples are shown in Figs. 9–12. The high-fidelity simulation of the spacecraft truth-model with which the system-id MEKF is being

tested includes: colored sensor noise, time-varying mass (fuel depletion), fuel-slosh dynamics, and the thermal-dynamics of the thruster warm-up model—including small random actuation delays.

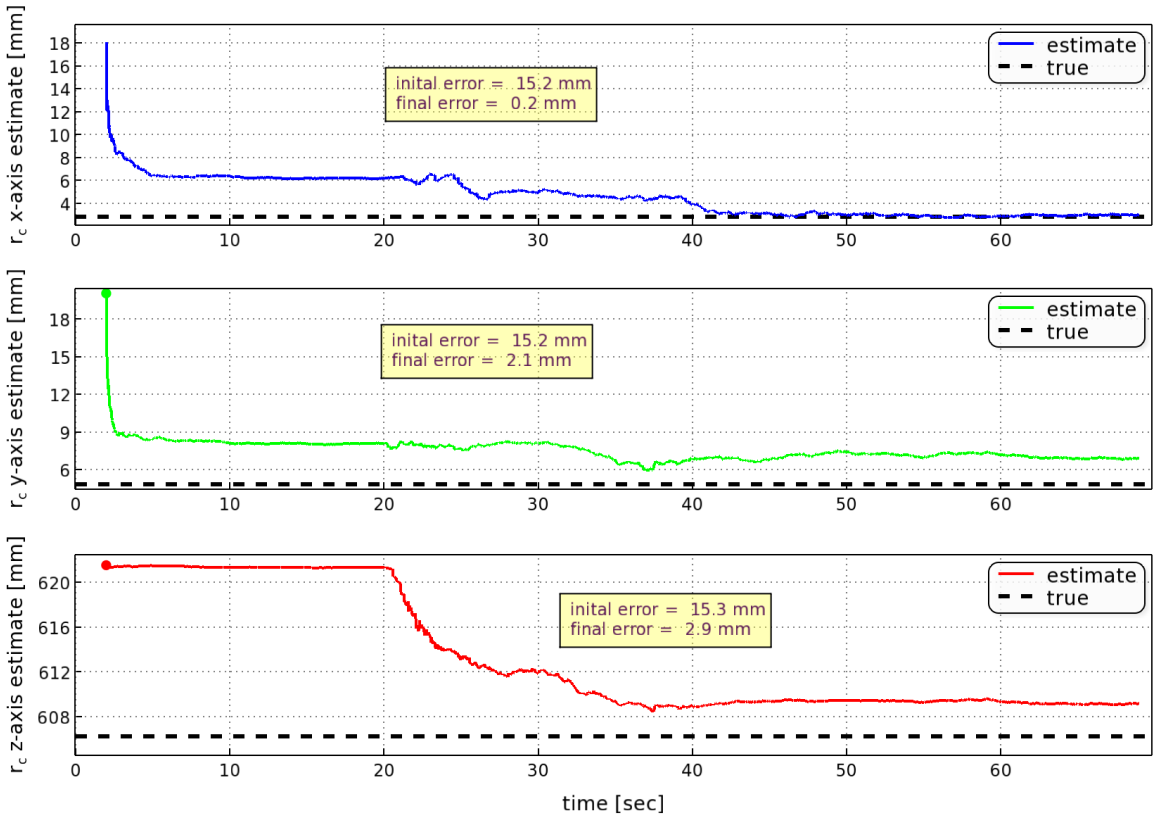

Figure 9. Observatory Center-of-Mass Estimation (Two-pulse sim)

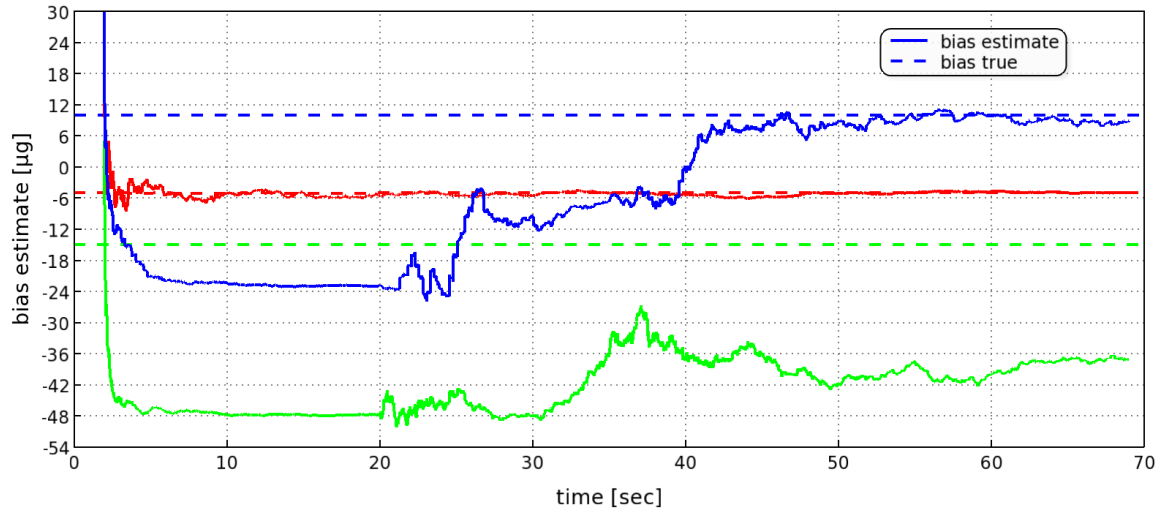

Figure 10. AMS Bias Estimation (Two-pulse sim)

Note that the results shown in Fig. 9 are for the total observatory center-of-mass—not just the fuel-mass that are the filter-states. Since the fuel-estimate has to potentially compensate for a number of parametric errors in the system, the total CM (and inertias) tend to be the more physically accurate result.

The bias estimates (Fig. 10) are also typical for MMS. The z-axis estimate tends to be the most accurate (which is actually the best possible result for the MMS application[1]), and the y-axis bias-estimate tends to be the least—most likely this is an artifact of the AMS placement relative to the spin-axis and center-of-mass. Nevertheless, bias estimation is not the primary goal of this filter, and the "tens of micro-g" error-regime of the estimate is sufficient for good system-id.

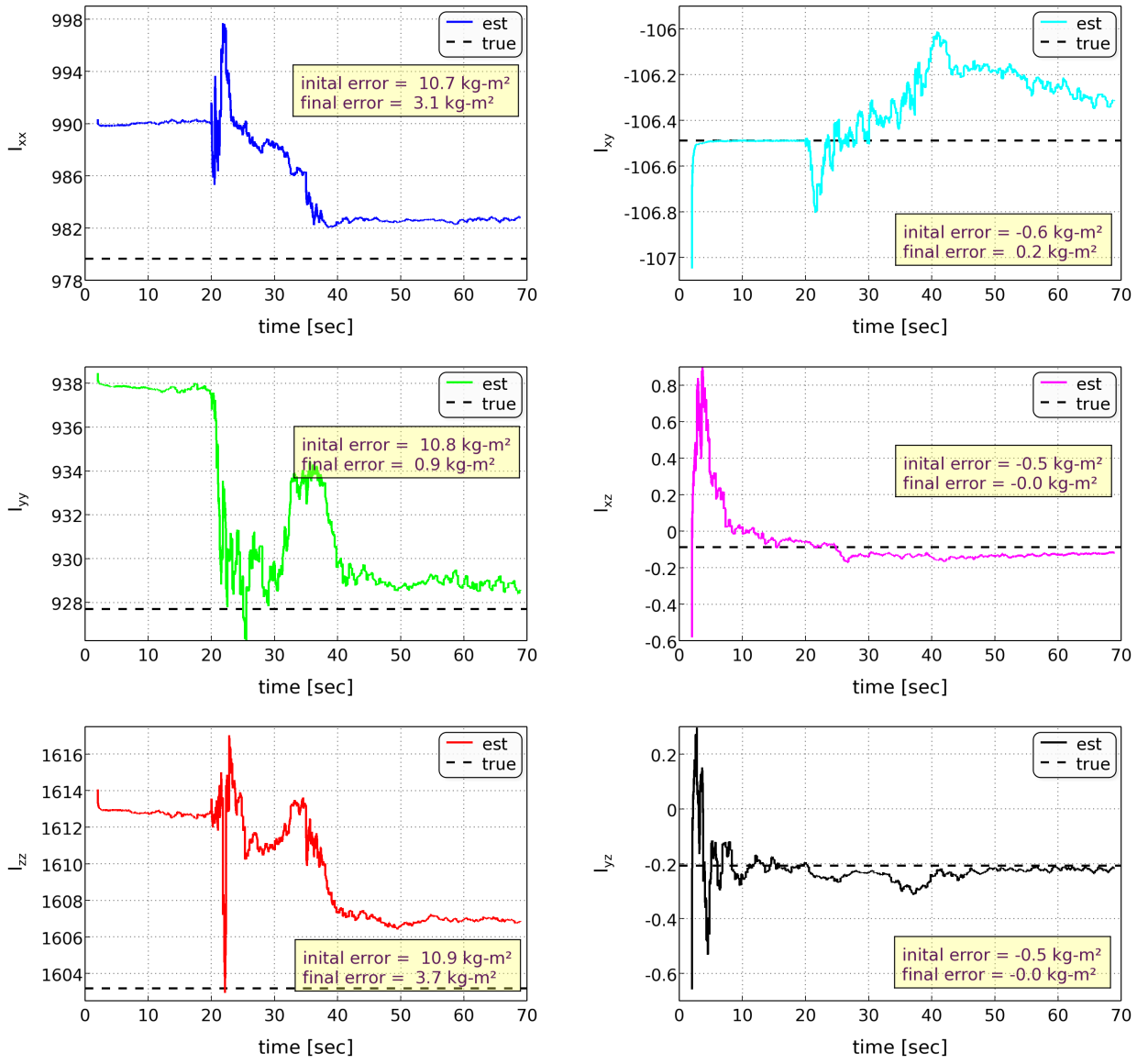

Figure 11. Observatory Moments and Products of Inertia Estimation (Two-pulse sim)

Figure 11 shows the evolution of inertia estimation process. This test-case shows that the I_{xz} and I_{yz} products of inertia are especially easy to identify on a spinner—a fact utilized on MMS to routinely perform a principal-axis (re)alignment as part of its pre-maneuver preparations[1].

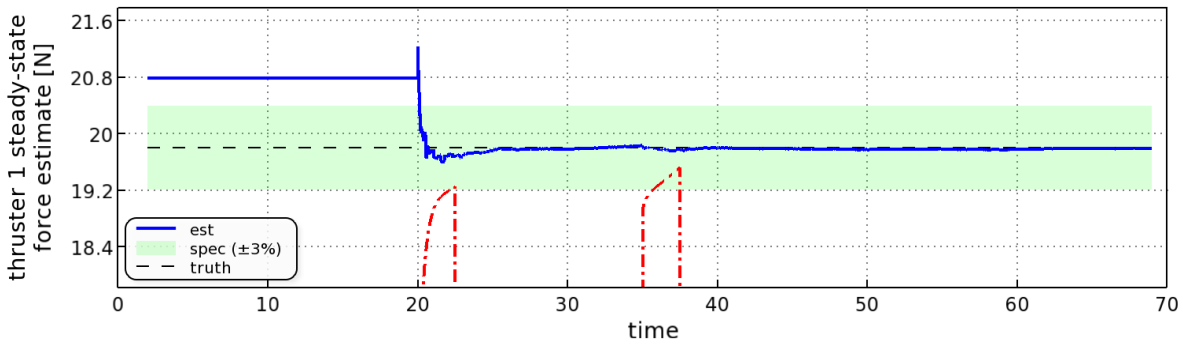

Figure 12. Thruster Steady-State Force Estimation (Two-pulse sim)

4.3.2 Flight Results

The angular rate estimates from the MMS1 ACS FSW for the full EA019 calibration maneuver are shown in Fig. 13. The stored real-time measurement data from the maneuver was processed by the off-line system-id MEKF in order to improve knowledge of the spacecraft's operational parameters. The new calibrated mass properties, and derived thruster duty-cycles were then uploaded into the ACS flight software. The process was repeated for all four observatories, which have been operating

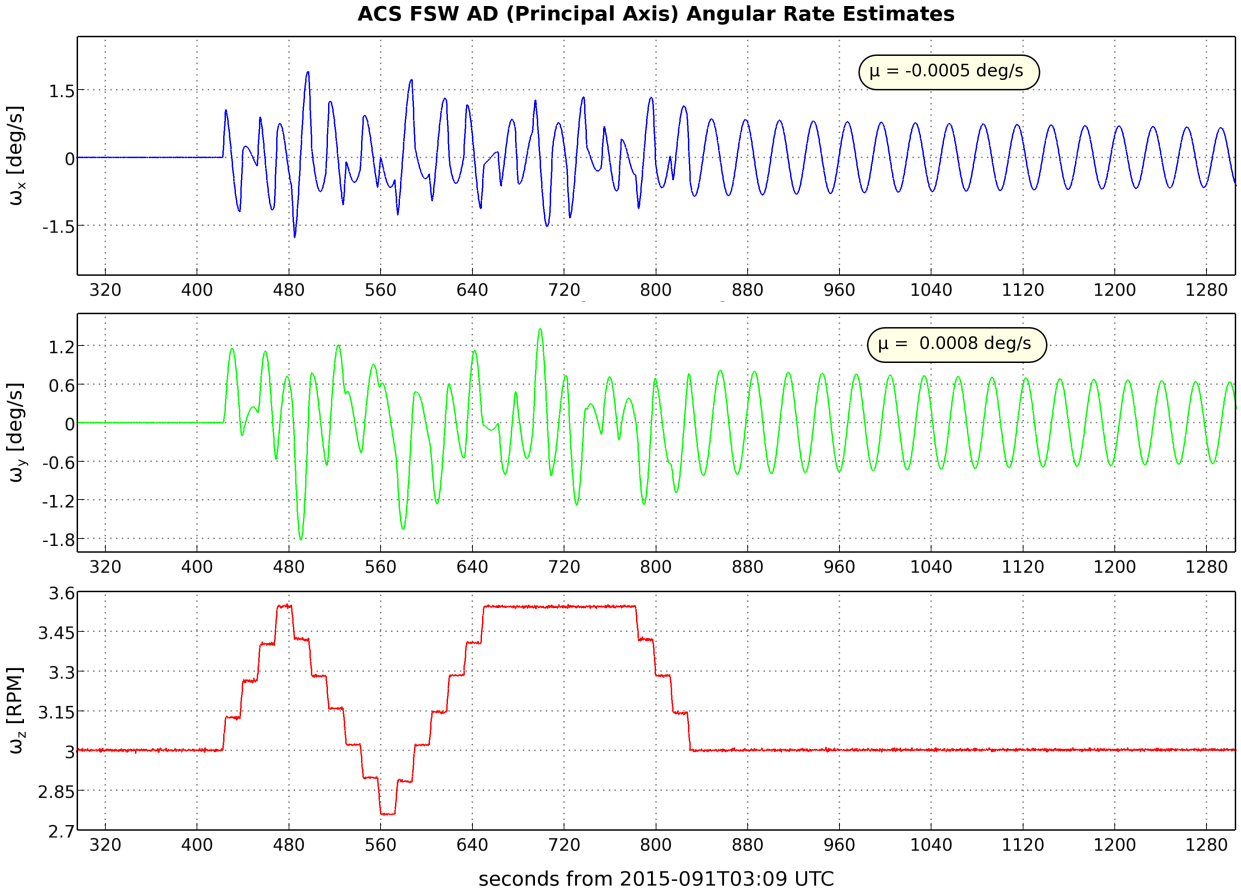

Figure 13. MMS1 ACS Estimated Angular Rate Telemetry (Full EA019 Maneuver)

successfully[9] using the updated coefficients since April 2015.

An example of the differences between the MMS1 pre-flight and post-calibration parameter estimates are given in Table 3. The excellent agreement attests to the effectiveness of the augmented-state filter, and the careful accounting of the spacecraft assembly process[13].

Table 3. MMS1 EA019 Calibration Results

Parameter	Units	Pre-launch	Post-Cal	Difference	
CM-x	mm	2.36	2.86	0.494	
CM-y	mm	5.03	4.96	-0.071	
CM-z	mm	607.68	606.43	-1.244	
Ixx	kg-m^2	977.15	975.33	-1.82	(-0.2%)
Iyy	kg-m^2	921.24	923.38	2.14	(0.2%)
Izz	kg-m^2	1594.99	1594.84	-0.15	(-0.0%)
Ixy	kg-m^2	-110.96	-106.48	4.47	(-4.0%)
Ixz	kg-m^2	-0.11	-0.09	0.02	
Iyz	kg-m^2	-0.25	-0.20	0.04	
Thrust-01	N	18.423	18.451		1.0799%
Thrust-02	N	18.286	18.334		1.0731%
Thrust-03	N	18.385	18.371		1.0753%
Thrust-04	N	18.329	18.321		1.0723%
Thrust-05	N	18.664	18.635		1.0907%
Thrust-06	N	18.727	18.712		1.0952%
Thrust-07	N	18.551	18.515		1.0837%
Thrust-08	N	18.425	18.385		1.0761%
Thrust-09	N	3.901	3.909		0.9153%
Thrust-10	N	3.926	3.938		0.9220%
Thrust-11	N	3.798	3.804		0.8907%
Thrust-12	N	3.868	3.879		0.9081%

5 Multi-body Dynamics

All of the filter development and flight results presented thus far have been based upon a rigid-body model of a spacecraft. For MMS, this was only a credible approximation during the commissioning period before the 60-meter long SDP wire-booms were deployed. Fortunately, the system identification maneuvers used to calibrate the mass properties and thrust were performed with the spacecraft in a semi-rigid configuration.

In fact, by using a de-tuned MEKF and a set of "effective" mass properties (extrapolated from our semi-stowed calibration results), the ACS flight software is able to continue to use its six-state MEKF otherwise unaltered. However, details of the multi-body dynamics extend beyond the scope of the present text. The topic of this estimator's performance with significant model-mismatch may instead become the focus of a future published work.

6 Summary

In this text, some of the fundamental principals regarding the use of a Multiplicative Extended Kalman Filter were re-introduced in the context of spacecraft attitude and rate determination for the MMS mission. The use of gyroscopes and the *gyro substitution* simplification in Extended Kalman Filters has become so ubiquitous, that this application stands out for its absence. The flight version of MMS's six-state attitude and rate filter—operating solely off star camera measurements—was then documented in full, with the hope that the (admittedly pedantic) exposition might help clarify some of the conceptual nuances surrounding the MEKF. At the very least, this paper hopes to call attention to the excellent reference texts and papers that have recently become available, while evangelizing on the conceptual "tidiness" of the MEKF formulation.

Additionally, the requirement for precise orbital maneuvering of the MMS formation belies the notion of a "simple spinner", and drives the need for precise knowledge of the observatories' mass properties and thrust-capabilities. A new estimator for system identification was presented that leveraged the flight MEKF framework—adding only high-rate accelerometer measurements and the desired quasi-constants as filter-states. With MEMS accelerometers becoming a fairly common component of a new generation of "CubeSats", the hope is that this off-line process proves a useful weapon in slaying the dragon of system identification that can torture a mission designer.

Finally, examples of the practical utility of the two filters was demonstrated using computer generated, and flight telemetered data. MMS's unqualified success with the flight filter—even using a relatively low-powered processor (by today's standards)—should further encourage the adoption of the MEKF as an aerospace staple.

7 Acknowledgments

The author would like to express sincere gratitude to Julie Thienel and F. Landis Markley, who's conference paper[12] was the genesis for this work, as well as for all their assistance with MEKF theory. Also, thanks go to J. Russell Carpenter's for his suggestion to use temporary *consider-states* while developing the MEKF code—it was a significant aid in filter-debug and tuning. Additionally, the author wishes to acknowledge the contributions of Suyog Benegalrao and Kathie Blackman, who were instrumental in processing the acceleration measurements in the ground-based system identification filter. They both remained tireless, and cheerfully determined—even in the face of mounting mission deadlines. Finally, thanks to Peter Kutt for his insights regarding optimizing the ACS flight software filter implementation, and Juan Raymond for finding the error originally in Eq. (67).

This work is dedicated to the memory of Nona Queen, who thankfully lived long enough to see the MMS mission succeed, and graciously overlooked the occasional missed Sunday phone calls home during the years while it was being built. Love you Mom. You are missed.

8 References

[1] Queen, S. Z., Chai, D. J., and Placanica, S. "Orbital Maneuvering System Design and Performance for the Magnetospheric MultiScale Formation." "AAS/AIAA Astrodynamics Specialist Conference," Vail, CO, August 2015. AAS 15-815.

[2] Queen, S. Z., Shah, N., Benegalroa, S. S., and Blackman, K. "Generalized Momentum Control of the Spin-Stabilized Magnetospheric Multiscale Formation." "AAS/AIAA Astrodynamics Specialist Conference," Vail, CO, August 2015. AAS 15-816.

[3] Markley, F. "Attitude Error Representations for Kalman Filtering." Journal of Guidance, Control, and Dynamics, Vol. 26, No. 2, pp. 311–317, 2003.

[4] Markley, F. and Crassidis, J. L. Fundamentals of Spacecraft Attitude Determination and Control. Space Technology Library. Springer, 1st edn., 2014.

[5] Lefferts, E. J., Markley, F., and Shuster, M. D. "Kalman Filtering for Spacecraft Attitude Estimation." Journal of Guidance, Control, and Dynamics, Vol. 5, No. 5, pp. 417–429, 1982.

[6] Crassidis, J. L. and Junkins, J. L. Optimal Estimation of Dynamic Systems. Chapman & Hall/CRC Applied Mathematics and Nonlinear Science Series. CRC Press, 2nd edn., 2012.

[7] Kutt, P. "Kalman Filter Optimizations for MMS." Tech. Rep. MMS-ACS-021, Goddard Space Flight Center, Greenbelt, MD, March 2011.

[8] Raymond, J. C., Sedlack, J. E., and Vint, B. "Attitude Ground System for the Magnetospheric MultiScale Mission." "25th International Symposium on Spaceflight Dynamics," Munich, Germany, October 2015.

[9] Chai, D. J., Queen, S. Z., and Placanica, S. J. "Precision Closed-Loop Orbital Maneuvering System Design and Performance for the Magnetospheric Multiscale Formation." "Proceeding of the 25th International Symposium of Space Flight Dynamics," Munich, Germany, October 2015.

[10] Van Loan, C. F. "Computing Integrals Involving the Matrix Exponential." IEEE Transactions on Automatic Control, Vol. 23, No. 3, pp. 395–404, 1978.

[11] Thienel, J. K. and Markley, F. L. "Comparison of Angular Velocity Estimation Methods for Spinning Spacecraft." "Advances in Astronautical Science," AAS/AIAA Guidance, Navigation, and Control Conference, 2011. AIAA 2011-6432.

[12] Thienel, J. K., Markley, F. L., and Harman, R. R. "Extended Kalman Filter for MMS State Estimation." "Advances in Astronautical Science," pp. 1513–1526. AAS/AIAA Space Flight Mechanics Meeting, 2009. AAS 09-202.

[13] Mariconti, S. "MMS Mass Properties Report." Tech. Rep. 461-MECH-RPT-0086, NASA/Goddard Space Flight Center, Greenbelt, MD, March 2015.

[14] Ramspacher, D. "Propellant Center of Mass Offset Memo." Tech. Rep. 461-PROP-CORR-0058, NASA/Goddard Space Flight Center, Greenbelt, MD, March 2015.

[15] Green, S. T. "Magnetospheric MultiScale Project Propellant Tank Slosh Testing and Modeling." Tech. Rep. 461-PS-RPT-0361 (18.15882), Southwest Research Institute, San Antonio, TX, 2012.

[16] Hughes, P. M. "NASA Goddard Space Flight Center FY 2006 Internal Research and Development Program." Tech. Rep. 2006-AR-V6, NASA/Goddard Space Flight Center, Greenbelt, MD, 2007.

[17] Rauch, H. E., Tung, F., and Striebel, C. T. "Maximum Likelihood Estimates of Linear Dynamic System." AIAA Journal, Vol. 3, No. 8, pp. 1445–1450, 1965.